2015

RuO2 Nanorods as an Electrocatalyst for Proton Exchange Membrane Water Electrolysis

Richard Smith
University of Vermont

RuO_2 Nanorods as an Electrocatalyst for Proton Exchange Membrane Water Electrolysis

A Thesis Presented

by

Richard Smith III

to

The Faculty of the Graduate College

of

The University of Vermont

In Partial Fullfillment of the Requirements
for the Degree of Master of Science
Specializing in Electrical Engineering

May, 2015

Defense Date: April 01, 2015
Thesis Examination Committee:

Walter Varhue, Ph.D., Advisor
Ting Tan, Ph.D., Chairperson
Micheal Cross, Ph.D.
Cynthia J. Forehand, Ph.D., Dean of Graduate College

Abstract

The desire for pure diatomic hydrogen gas, $H_2(g)$, has been on the rise since the concept of the hydrogen economy system was proposed back in 1970. The production of hydrogen has been extensively examined over 40 + years as the need to replace current fuel sources, hydrocarbons, has become more prevalent. Currently there are only two practical and renewable production methods for hydrogen; landfill gas and power to gas. This study focuses on the later method; using various renewable energy sources, such as photovoltaics, to provide off-peak energy to perform water electrolysis. Efficient electrolysis takes place in electrochemical cells which maximize performance efficiency with the use of noble metal electrocatalyst. Optimizing these electrocatalyst to be less material dependent, highly durable, and more efficient will support the implementation of power to gas electrolysis into the energy infrastructure.

The main focus of this study is to explore RuO_2 nanorods as a possible electrocatalyst for Proton Exchange Membrane (PEM) water electrolysis. A PEM electrolyzer cell has been constructed and fitted with a RuO2 nanorod decorated, mixed metal oxide (MMO) ribbon mesh anode catalyst structure. The current density-voltage characteristics were measured for the RuO2 nanorod electrocatalyst while under water feed operation. The electrocatalytic behavior was compared to that of ribbon mesh anode catalyst structures not decorated with RuO_2 nanorods; one coated with a Ir/Ta MMO catalyst, the other was stripped of the MMO coating resulting in a Ti ribbon mesh anode. The results of these experiments show increased activity with the RuO_2 nanorod electrocatalyst corresponding to a decrease in electrochemical overpotential. Through the collection of experimental data from various electrolyzer cell configurations, these overpotentials were able to be identified, resulting in categorical attributions of the enhanced catalytic behavior examined.

Acknowledgements

I would like to thank Dr. Wally Varhue for advising me and providing insightful advise, encouraging support, and the opportunity to study energy storage technology. I would like to thank Dr. Mike Cross for his involvement, the growth and imaging of the RuO_2 nanorods, and especially the quick responses to questions during a busy semester. Dr. Ting Tan provided valuable feedback and support. Finally I would like to thank the Vermont Space Grant Consortium / VT-NASA EPSCoR for financial support, which without this study would not have been possible.

Dedication

For the future of Energy.

Table of Contents

List of Figures

Chapter 1

Introduction

1.1 Purpose

The current global reliance on fossil fuels is causing economical, environmental, and social problems which are threatening the future of mankind and the planet. Recent advancements in alternative energy generation have been shedding new hope for keeping our current technological era above water while restoring peace and harmony to the planet's social and environmental well being. The major hurdle faced by virtually all renewable technology today is its inability to support base load demand [1]. The current grid power systems can compensate for changes in load throughout the day, especially when loads reach peak, for example in the late afternoon when everyone comes home from work to make dinner or watch television. Energy generated from natural sources such as wind and solar cannot be controlled or called upon for when peak loads occur. There is a demand for a clean system that can economically store renewable energy to meet peak demand. Hydrogen production has been considered to be such an energy storage mechanism that can be made to work with the current energy infrastructure. Atomic hydrogen does not occur naturally, and must be produced by endothermic processes such as electrolysis in a proton exchange membrane (PEM) type cell [2]. Research is increasingly focusing on the development of

PEM electrolysis by various means [3].

Current PEM electrolyzer cells operate at high efficiencies requiring the use of expensive electrocatalysts. Electrocatalyst development is an area receiving increased attention due to the scarcity and high costs of the noble metals. The recent societal fixation of electronic devices, such as smartphones, has increased the demand of the leading noble metals, such as Ir, Pt, and Pd. Since Ir is one of the rarest elements in the Earth's crust, there is a need to develop an electrocatalyst for PEM water electrolysis that is more sustainable [4].

1.2 Proton Exchange Membrane Electrolysis of water

1.2.1 Overview

The method of hydrogen gas production employed in this study is the electrolysis of water using a proton exchange membrane (PEM) electrolyzer cell. This requires applying an electrical voltage to water and decomposing it into its core elements; oxygen and hydrogen. The overall chemical equation is as follows:

$$2H_2O \rightarrow 2H_2 + O_2 \tag{1.1}$$

The PEM electrolyzer cell is divided into three major components; the anode, the cathode, and the membrane electrode assembly (MEA). The process of water electrolysis consist of two half reactions which take place at physically divided locations, the anode and cathode. Each of these sections are composed of various components which facilitate this process. The oxygen evolution reaction (OER) occurs at the anode:

$$2H_2O \rightarrow O_2 + 4H^+ + 4e^- \tag{1.2}$$

The anode consists of a bipolar plate usually made of graphite or some metal, machined to supply water to the MEA, where the reaction occurs, while also providing an exit path for the O_2 byproduct. This bipolar plate is also where a positive voltage bias is applied to provide the necessary free energy of the OER (1.23 eV) [5].
The cathode is the location where the hydrogen reduction reaction (HRR) occurs:

$$4H^+ + 4e^- \rightarrow 2H_2 \tag{1.3}$$

The cathode consists of a bipolar plate similar to the anode bipolar plate. It functions the same way, supplying water to the MEA while providing an exit path for the H_2 product. This bipolar plate is also where a negative voltage bias is applied to provide the necessary flow of electrons required for the reaction to occur.

These electrochemical reactions occur at a specific location called the three-phase boundary layer which is located in the heart of the MEA. Most conventionally, MEAs consist of five layers and are thus called 5-Layer MEAs [6]. The composition of a 5-Layer MEA is as follows; the center layer consists of a proton conductive membrane, commonly Nafion, which allows the movement of hydronium atoms (H_3O^+) from the anode to the cathode. On either side of this membrane (anode and cathode sides) an electrode layer is present containing the electrocatalysts which facilitate the electrochemical reactions. Covering each electrode layer is a porous gas diffusion layer (GDL) which allows the reactant gases to flow freely to and from reaction sites while also providing electrical connection between the electrocatalyst layer and bipolar plates.

PEM water electrolysis begins with a feed of water to the positively biased anode bipolar

plate. As the water flows through the bipolar plate it is uniformly delivered to the MEA. The first layer of the MEA, the GDL, allows mostly gaseous water vapor to pass through to the electrode layer, keeping the liquid water from collecting and 'flooding' the electrocatalyst. Once the gaseous water reaches the electrocatalyst layer it is oxidized. The electrochemical reaction involves three kinds of species, gases, electrons, and protons, and therefore can only occur on an area of the electrode surface where all three species exist and have access. This three-phase boundary layer is where the gaseous water oxidizes via the required free energy of the OER, and the resulting oxygen gases, hydronium ions (protons), and electrons all have modes of dispersion [6]. The oxygen gas product exits back out through the GDL to the bipolar plate, while the hydronium ions pass through the proton conductive Nafion membrane. The electrons travel through the GDL to the bipolar plates, aided by the applied bias. The electrons ultimately conduct to the cathode bipolar plate. As the hydronium ions pass through the membrane they are met on the cathode side at a similar three-phase boundary layer by the electrons which have traveled from the cathode bipolar plate through the GDL. Here the hydrogen reduction reaction occurs and the resulting hydrogen gases pass through the GDL, exiting the cathode bipolar plate. Faraday's first law of electrolysis relates the hydrogen gas (H_2) produced to the current across the bipolar plates [7]. Figure 1.1 [8] displays a theoretical PEM electrolysis process powered by a photovoltaic cell.

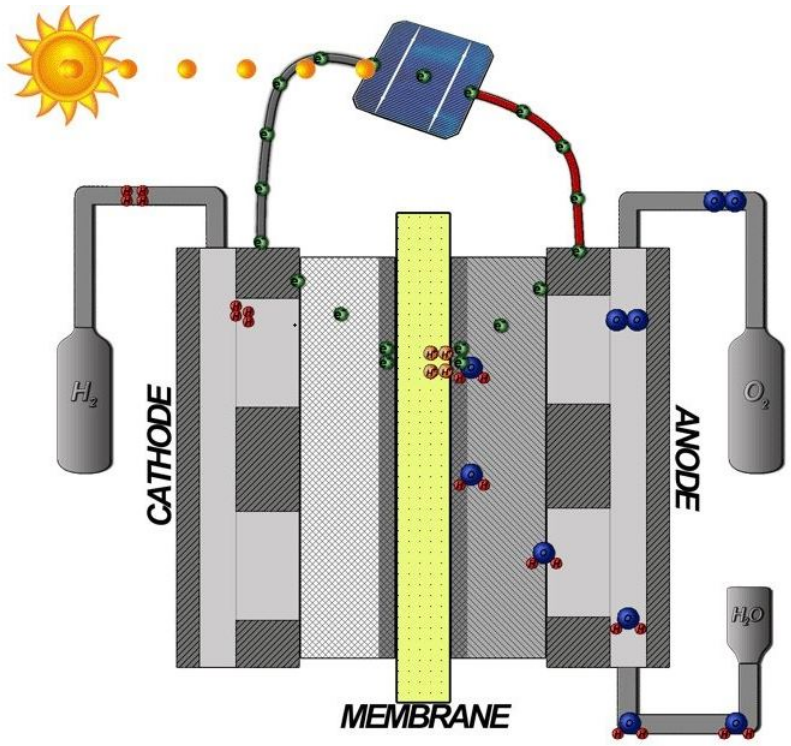

Figure 1.1: PEM electrolysis

1.2.2 The Nafion Membrane

The transport of hydronium ions through the Nafion membrane is an essential process of PEM water electrolysis. Although this study does not focus specifically on the Nafion membrane, the mechanism of transport is a fundamental concept of the electrolysis process and thus will be explained in the following section.

Nafion is a sulfonated tetrafluoroethylene based fluoropolymer-copolymer. It has unique ionic properties which are a result of it's specific molecular structure. Nafion is made up of a tetrafluoroethylene backbone, commonly known as Teflon, onto which perfluorovinyl ether groups are terminated with sulfonate groups [9]. The molecular formula is as follows

$$C_7HF_{13}O_5S.C_2F_4.$$

Nafion is the material used most commonly as the proton conductor for PEM fuel cells and electrolyzer cells because the Teflon backbone provides thermal and mechanical strength while the sulfonate groups provide proton conductivity when hydrated. There are three universal observation of the morphology of Nafion that govern an understanding of proton transport [10]. Nafion is separated into two distinct phase regions which are hydrophobic and hydrophilic. The Teflon backbone makes up the hydrophobic region while the hydrophilic region is made up of the sulfonated groups, which, when hydrated, change size and shape, eventually creating a continuous network upon which water and protons utilize as a mechanism of transport. Figure 1.2 shows this hydronium transport mechanism.

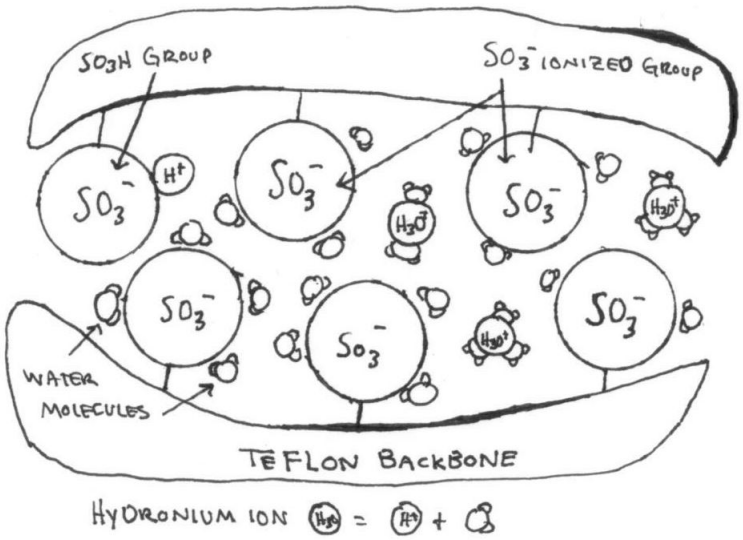

Figure 1.2: Transport mechanism of hydronium ions H_3O^+ through Nafion membrane

Water plays an essential role in the PEM electrolysis process. The proton conductivity of the Nafion membrane can approximately vary by six orders of magnitude depending on

hydration conditions [11]. Drying out of the membrane results in poor proton conductivity ultimately causing low hydrogen production and inefficient performance. Though it seems keeping the membrane hydrated in a PEM electrolyzer cell is trivial, diffusion of water across the membrane can cause an imbalance and the result in heat generation from the electrochemical reaction promotes membrane dehydration. In fact, the proton exchange membrane is a region that requires a delicate balance. Where a lack of water can cause poor transport, an excess of water can cause an obstruction of the electrochemical process. This phenomena, called flooding, is a result of liquid water forming on the electrocatalyst surface, causing a decrease in exposed surface area, limiting the available reaction sites. The water essentially becomes a barrier, blocking the transport of reactants to sites where the electrochemical reactions occur. Nafion has been researched extensively as a membrane material in PEM fuel cells, though the hydration state of Nafion differs between PEM fuel cell operation and electrolysis operation. In theory this would create different boundary conditions though the water uptake and performance of the membrane may or may not be effected, as there is contradictory evidence in the literature [3].

1.2.3 Electrochemical Reactions

The electrochemical reactions involved in the electrolysis process can be described by an electrical charge transfer and a change in the Gibbs Free Energy [6]. The electrical energy ($W = IV\Delta t$) required to split one mole of water in an equilibrium state is equivalent to the water dissociation reaction's change of Gibbs Free Energy (ΔG_d). This change of Gibbs Free Energy is determined by the thermodynamic potentials of the electrochemical reaction. The reaction requires energy for the dissociation of the water molecule and the energy expanded by the production of gases; hydrogen and oxygen. Both of these energy components are included in the thermodynamic potential change in enthalpy of water ($\Delta H = 285.8kJ$).

This change in enthalpy is the energy required to perform water electrolysis, though it is not necessary to provide the total energy in the form of electricity because the thermodynamic potential entropy of each reactant can be supplied in the form of heat. Entropy is a function of temperature and therefore the environment in which the reaction is occurring contributes to the change in entropy ($T\Delta S$). The resulting amount of energy required for the dissociation reaction to occur is the difference of enthalpy and entropy as represented in the following equation:

$$\Delta G_d = \Delta H - T\Delta S \tag{1.4}$$

where:

ΔG_d is the dissociation reaction's change of Gibbs free energy.

ΔH is the change in enthalpy.

ΔS is the change in entropy of the reactants which is a function of temperature T.

The above equation shows the Gibbs Free Energy of the dissociation reaction is a function of temperature. If the maximum amount of heat energy is supplied, $T\Delta S = 48.6\frac{kJ}{mol}$, then ΔG_d is minimized to $237.2\frac{kJ}{mol}$ which is the case at 25°C under standard conditions [12]. Gibbs Free Energy can be used in the following relationship to calculate the voltage required to perform electrolysis.

$$\Delta V = \frac{\Delta G_d}{nF} \tag{1.5}$$

where:

ΔG_d is the dissociation reaction's change of Gibbs free energy.

n is the number of electrons transferred (2 for water)

F is the Faraday Constant (96,485 $\frac{C}{mol}$)

The minimum voltage can be calculated using the Gibbs Free Energy at standard conditions:

$$V_{min} = \frac{\Delta G_d}{nF}$$
$$V_{min} = \frac{237{,}200 J mol^{-1}}{(2)(96{,}485 C mol^{-1})}$$
$$V_{min}\text{=1.23 volts}$$

This calculated thermodynamic voltage only pertains to an ideal case without any loss due to a change in entropy. In practice, losses can occur due to internal resistances in the cell as well as various overpotentials. The operating voltage required to drive an electrolysis cell at a given current I can be expressed as:

$$V_{op} = V_{min} + IR + \sum V_o \tag{1.6}$$

where:

R is the internal resistance of the electrolysis cell.

$\sum V_o$ is the sum of the overpotentials.

Optimal electrolysis occurs in cells designed to minimize internal resistance between system components as well as choosing materials which produce minimal overpotential.

1.2.4 Overpotential

The calculated voltage required for the electrolysis reaction to occur is the theoretical value ($V_min = 1.23V$) when, in practice, the required voltage is higher due to losses in the system, as well as nonidealities in the electrochemical process. These addition voltage requirements are called overpotentials (V_o) and can be determined experimentally by subtracting the operating voltage of the cell from the calculated thermodynamic voltage minimum

($V_{min} = 1.23V$), as shown in the equation above. The voltage efficiency is defined as the ratio of the thermodynamic voltage to the cell's operating voltage which includes the overpotential. The equations for voltage efficiency are as follows:

$$V_o = V_{op} - V_{min} \tag{1.7}$$

$$\eta_v = \frac{V_{min}}{V_{op}} \tag{1.8}$$

where:

η_v is the Voltage Efficiency.

V_{min} is the thermodynamic voltage under standard conditions.

V_{op} is the Cell Operating Voltage.

Combining the above equations results in an expression for voltage efficiency as a function of overpotential, as shown in Equation 1.9.

$$\eta_v = \frac{V_{min}}{V_{min} + V_o} \tag{1.9}$$

In electrochemical reactions there are a variety of overpotentials that tend to be categorized in ambiguous subcategories due to the difficulty to associate portions of measured overpotential to a specific source. There are three main categories of which overpotential is grouped into; activation, resistance, and mass transport. Current electrolyzer cells experience the greatest overpotential resulting from the OER which occurs at the anode. Reaction overpotential is a less ambiguous subcategory of activation overpotential that specifically relates to chemical reactions that precede electron transfer [13]. The reaction overpotential can be significantly reduced with the use of an electrocatalyst. Popular OER electrocatalyst materials are RuO_2 and IrO_2 since these oxides exhibit the lowest reaction overpotentials [3]. At the cathode, the HRR, which produces hydrogen, can be facilitated with almost no overpotential by a platinum electrocatalyst. The relief of these overpoten-

tials affect the electrochemical reaction rate and the related current densities. The kinetics of the electrocatalyst play a major role in the overall voltage efficiency of an electrolyzer cell and are therefore one the most studied components of the electrolysis system.

1.3 Importance of The Electrocatalyst

1.3.1 Overview

As previously stated, electrolysis of water is a process consisting of two half-reactions; oxygen evolution and hydrogen reduction, which take place on different sides of the PEM electrolyzer cell, the anode and cathode respectively. Oxygen evolution is the only reaction that requires the input of energy to occur, making it a focused topic of research. It has been shown that the required minimum thermodynamic voltage to drive this reaction increases in practice due to various experienced overpotentials. Electrocatalyst reduce overpotentials in various ways such as providing optimal electrical conductivity, increasing available reaction sites, or enhancing exchange current densities. It has been determined that these electrocatalytic abilities are exhibited by specific materials in different environments [14]. Current studies of IrO_2 and RuO_2, which have exhibited the lowest measured overpotentials for water electrolysis, aim to increase electrocatalytic properties of these materials in order to further advance electrocatalytic water electrolysis. This section will explain the kinetic theory of the electrocatalytic reactions which relate to this study.

1.3.2 Electrochemical Kinetics

The fundamental kinetics that govern the electrochemical reactions provide insight to organizing the results of experimental studies and information about reaction mechanisms.

Consider the reaction given below :

$$A \rightleftharpoons B \tag{1.10}$$

The rate of the forward and backward reactions, ϕ_f and ϕ_b respectively, are expressed in the following equations in terms of the rate constants, k_f and k_b, and the concentration of species, C_A and C_B.

$$\phi_f = k_f C_A \tag{1.11}$$

$$\phi_b = k_b C_B \tag{1.12}$$

The net rate, ϕ_{net}, is defined as the difference of the forward and backward reaction rates.

$$\phi_{net} = \phi_f - \phi_b = k_f C_A - k_b C_B \tag{1.13}$$

A state of equilibrium is defined as the point in which the rate of the forward reaction is equal to the rate of backward reaction. In this case the equation above can be expressed as:

$$\frac{k_f}{k_b} = \frac{C_A}{C_B} \tag{1.14}$$

An equation similar to the one above is required of all kinetic theory. That is, for a kinetic expression to be valid, reduction to thermodynamic equations at equilibrium is essential. In some ways, this requirement is similar to a boundary condition.

The Arrhenius Equation shown below is an expression for the rate constant of a reaction, k, which follows the experimental fact that the natural log of most solution-phase reactions

vary linearly to the inverse of temperature.

$$k = Aexp\left[\frac{-E_A}{RT}\right] \tag{1.15}$$

E_A represents the activation energy or energy barrier that must be overcome for the reaction to occur. Therefore the whole exponential term expresses the probability the energy barrier will be surmounted and A, the frequency factor, is the number of attempts required before the energy barrier is overcome. The following section describes activation energy and how it is affected by catalyzed reactions.

1.3.3 Oxygen Evolution Reaction Activation Energy

It is advantageous to have the oxygen evolution reaction (OER) occur at potentials as close to the thermodynamic minimum voltage ($V_{min} = 1.23V$) as possible while maximizing the reaction rate. The OER cannot take place until all reactants have acquired the energy needed to stretch, bend, or otherwise distort one or more bonds. This critical energy is known as the activation energy of the reaction. An activation energy diagram of the kind shown in Figure 1.3 plots the total energy of a reaction system as it proceeds from reactants to products [15].

The ΔH term represents the change in enthalpy of the reactants compared to the enthalpy of the products. This figure shows the effect a catalyst has on the activation energy of the reaction, E_{ac}. It is important to note that the catalyst only affects the activation energy and thus the rate of the reaction, not the thermodynamic change in enthalpy (ΔH).

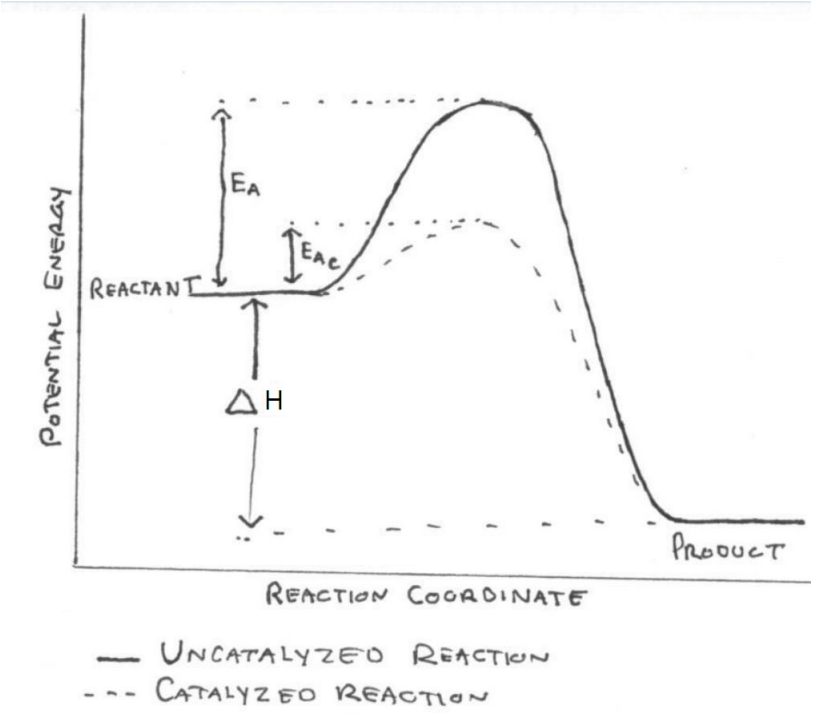

Figure 1.3: Activation Energy Diagram

1.3.4 Kinetic Theory

The rate of an electrochemical reaction is commonly expressed in terms of the current density (J), with units $\frac{mA}{cm^2}$. An expression for the rate typically begins with the derivation of a more general relationship know as the Butler-Volmer Equation.

In electrochemistry the general reversible electrode reaction is expressed as a redox reaction show in the following equation.

$$O + ne = R \tag{1.16}$$

This reaction is governed by the thermodynamic Nernst Equation at equilibrium (Equa-

tion 1.17). This equation can be used to relate the operational potential, V_{op}, of the electrode to the concentration of reactants and products in the solution.

$$V_{op} = V_{min} - \frac{RT}{nF} ln \left(\frac{C_R^*}{C_O^*} \right) \tag{1.17}$$

The Nernst Equation can be applied to develop a greater understanding of the rate of the reaction constants, k_f and k_b, for a state of equilibrium, where $\phi_f = \phi_b$. Applying Equation 1.14 to the redox reaction in Equation 1.16 results in the following expression.

$$k_f C_O(0,t) = k_b C_R(0,t) \tag{1.18}$$

$C_O(0,t)$ and $C_R(0,t)$ represent the concentrations of species on the electrocatalyst surface which is equal to the concentration of species in the solution at equilibrium. The following equation is the result of taking the natural log of both sides of the above equation rearranged:

$$ln(k_b) - ln(k_f) = ln \left(\frac{C_O(0,t)}{C_R(0,t)} \right) \tag{1.19}$$

Since this equation is based on equilibrium conditions, the Nernst Equation (Equation 1.17) can be applied.

$$ln(k_b) - ln(k_f) = ln \left(\frac{C_O(0,t)}{C_R(0,t)} \right) = \frac{nF}{RT}(V_{op} - V_{min}) \tag{1.20}$$

Differentiating this equation with respect to V_{op} results in the symmetrical equation of the rate constants.

$$\frac{RT}{F} \left(\frac{d}{dV_{op}} ln(k_b) + \frac{d}{dV_{op}} ln(k_f) \right) = 1 \tag{1.21}$$

This equation defines the charge transfer coefficient α which is the measure of the symmetry

of the energy barrier. Where:

$$\alpha = \frac{RT}{F}\left(\frac{d}{dV_{op}} ln(\frac{1}{k_f})\right) \tag{1.22}$$

and the symmetry factor of the backward reaction is $1 - \alpha$.

$$1 - \alpha = \frac{RT}{F}\left(\frac{d}{dV_{op}} ln(k_b)\right) \tag{1.23}$$

Figure 1.4 shows the effect various α values have on a general activation energy diagram. An increase in α increases the forward reaction rate and a decrease in α increases the backward reaction.

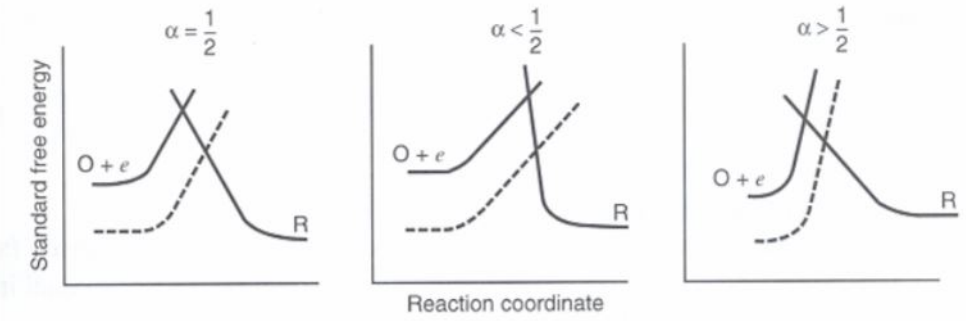

Figure 1.4: α Affect on Activation Energy Diagram

Integrating the two symmetry equations results in expressions of the reaction rates.

$$ln\left(\frac{1}{k_f}\right) = \frac{\alpha F V_{op}}{RT} + C \tag{1.24}$$

By continuing the application of equilibrium conditions, the constant C can be defined as the standard rate constant k_f^o, where $k_f = k_f^o$ when $Vop = Vmin.$ the previous equation becomes:

$$k_f = k_f^o exp\left[\frac{-\alpha F(V_{op} - V_{min})}{RT}\right] \tag{1.25}$$

The backward reaction rate can similarly be expressed:

$$k_b = k_b^o exp\left[\frac{(1-\alpha)F(Vop - V_{min})}{RT}\right] \tag{1.26}$$

1.3.5 The Butler-Volmer Equation

The Bulter-Volmer Equation of electrode kinetics links four important parameters; faradaic current, electrode potential, and both concentration of reactants and products. The equation can be derived by applying Equations 1.25 and 1.26 to Faradays Law.

Equation 1.27 is an expression of Faradays Law which states current density of an electrochemical reaction is proportional to the transfer of charge and the rate of reactions.

$$J = nF\phi \tag{1.27}$$

Applying Equation 1.13 to the above equation results in an expression of current density in terms of reaction rate constants, k_f and k_b, and the concentrations of reactants and products.

$$J = nF(k_f C_O^* - k_b C_R^*) \tag{1.28}$$

Substituting the derived expressions of the rate reaction constants from Equations 1.25 and 1.26 into the above equation results in the following equation.

$$J = nF\left(k_f^o C_O(0,t) exp\left[\frac{\alpha_O F(V_{op} - V_{min})}{RT}\right] - k_b^o C_R(0,t) exp\left[\frac{\alpha_R F(V_{op} - V_{min})}{RT}\right]\right) \tag{1.29}$$

Where the charge transfer coefficient of the oxidation reaction is defined as $\alpha_O = \alpha$, and the charge transfer coefficient of the reduction reaction is defined $\alpha_R = 1 - \alpha_O$. Applying the equilibrium case to the equation above, in which both forward and backward reactions

occur at the same rate, $J = 0$, the rate of the reactions can be defined as the exchange current density, J_o, which is expressed in the following equation.

$$J_o = nFk_f^o C_O^* exp\left[\frac{\alpha_O F(V_{op} - V_{min})}{RT}\right] = k_b^o C_R^* exp\left[\frac{\alpha_R F(V_{op} - V_{min}}{RT}\right] \tag{1.30}$$

The Bulter-Volmer Equation is derived by combining Equations 1.29 and 1.30 expressed in the following equation.

$$J = J_o\left(\frac{C_O(0,t)}{C_O^*} exp\left[\frac{\alpha_O F(V_{op} - V_{min})}{RT}\right] - \frac{C_R(0,t)}{C_R^*} exp\left[\frac{\alpha_R F(V_{op} - V_{min})}{RT}\right]\right) \tag{1.31}$$

This equation is a general relationship between the current density and voltage overpotential of a electrochemical reaction with consideration of both the forward and backward reactions. The equation is valid for both the anode and cathode of an electrochemical cell. Specifically for a PEM water electrolyzer cell the minimal voltage for the anode oxidation reaction is $V_{min} = 1.23V$ and for the cathode reduction reaction is $V_{min} = 0$.

Applying the Butler-Volmer Equation to the electrochemical reactions of a PEM water electrolyzer cell results in an expression of the current density for both the anode and cathode electrodes. The operation of the electrolyzer cell requires the oxidation reaction of water to be the dominate reaction occurring at the anode and the reduction reaction of the hydronium ion to be the dominate reaction occurring at the cathode. Therefore the current density experienced at the anode and cathode can be expressed in the following equations respectively.

$$J_A = J_{oA}\left(exp\left[\frac{\alpha_O F(V_{op} - V_{min})}{RT}\right]\right) \tag{1.32}$$

$$J_C = -J_{oC}\left(exp\left[\frac{\alpha_R F(V_{op} - V_{min})}{RT}\right]\right) \tag{1.33}$$

The Tafel Equation, Equation 1.34, is ultimately the general expression of the above equations relating the current density to overpotential for a forward or backward reaction occurring on a single electrode where the overpotential is defined as the difference of the operating potential, V_{op}, and minimum potential, V_{min}, from Equation 1.7.

$$J = J_o exp\left[\frac{V_o \alpha F}{RT}\right] \tag{1.34}$$

The exchange current density, J_o, represents the intrinsic rate of electron transfer for a certain electrode material, where as the charge transfer coefficient, α, indicates the interfacial potential experienced by the ion. Therefore, both electrode material and electric field determine the reaction rate [16].

The exchange current density is a measure of interaction between the electrode and the reactants, of which heavily depends upon the rate constant and surface concentrations of the electrochemical reaction. The exchange current density is an important parameter in calculating the activation overpotential. It represents the electrode's readiness to proceed with the electrochemical reaction. High exchange current density means high reactivity of the electrode [17]. It is the frequency factor of the Tafel Equation.

The charge transfer coefficient represents the effect an interfacial electrical potential has on the free energy barrier of the electrochemical reaction [18]. An interfacial electric field occurs on the electrode surface which contributes to the activation of ions or electrons to overcome the free energy barrier. The charge transfer coefficient determines the potential provided by the interfacial electric field, and is dependent upon the electrode-reactant interface. In a solid-liquid interface for example, a double layer (DL) is formed on the surface of the electrode. First described by Hermann von Helmholts in 1853, the electric double layer is essentially a molecular dielectric that stores charge electrostatically and is thus commonly

represented in electrolyzer models as a parallel plate capacitor [19]. Specifically at the reaction site, the DL is a common boundary or interface experienced between the positively charged anode electrocatalyst and the H_2O reactant. See Figure 1.5. This electrostatic field terminates on oppositely charged ionic species in the dielectric fluid. The thickness of this DL or, in this case the polarized H_2O molecules, is expected to be in the range of a few nanometers [19], and is uniformly distributed across any surface that comes in contact with the electrolyte. The voltage drop across the DL has been predicted by Gouye Chapman Theory of the solid-liquid interface [20].

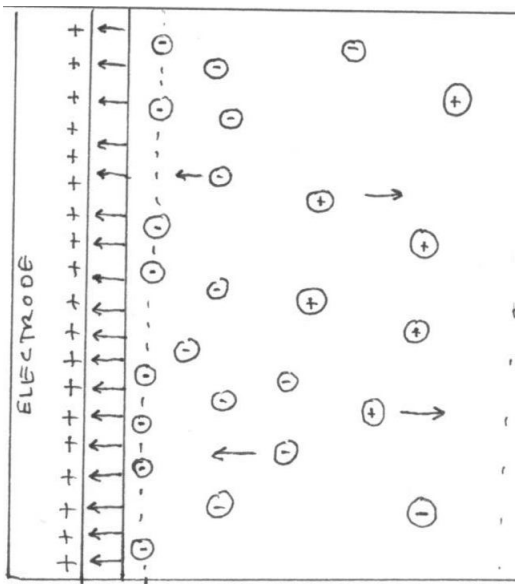

Figure 1.5: Helmholts Double Layer

The exchange current density and charge transfer coefficient govern some of the fundamental relationships of electrochemical kinetics. The Tafel Equation, shown in Equation 1.34, represents a mathematical relationships between current density and overpotential. The equation shows that an increase in both of the previously described parameters, J_o and α, lower the overpotential of the electrochemical reaction. The theory of how exchange

current density and charge transfer contribute to the Tafel Equation provide greater understanding to the electrocatalytic effect on activation energy. A similar relationship can be derived from the quantum mechanical theory of the OER. The following section describes this connection.

1.3.6 Quantum Mechanical Theory of Electrochemical Reactions

Water electrolysis involves the transfer of electrical charge from one atomic species to another. This physical process can best be described by the quantum mechanic potential well concept, Figure 1.6 depicts this concept. The electron in the atomic species is depicted as a particle in a one-dimensional potential well. The height of the well represents the free energy barrier the electron must overcome to move to the energy level in the product species [21]. A conceptual connection can be made between this free energy barrier and the activation energy. The easier the free energy barrier can be passed the more efficient the OER. Figure 1.6 shows the effect of an external electric field on a quantum potential well, as described be the Quantum Confined Stark Effect (QCSE) [22]. As the figure shows, the electric field skews the potential well resulting in a change in symmetry of the free energy barrier and an enhanced tunneling effect. This could be related to the affect of the charge transfer coefficient, α, described earlier; a lower overpotential is experienced when a greater potential gradient is provided by the interfacial electric field. This theory supports the implementation of RuO_2 nanorods as an electrocatalyst material for the OER.

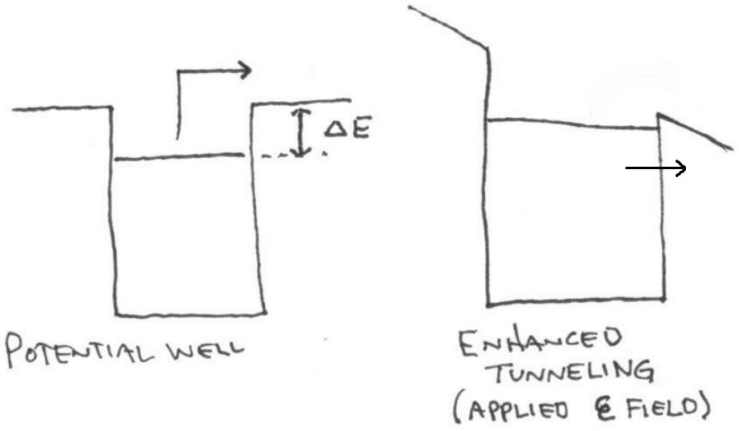

Figure 1.6: Enhanced Tunneling Effect Due to applied electric field ϵ

1.3.7 Mass Transfer Consideration

In order to develop an efficient data analysis method, a more complete current density to voltage overpotential relationship can be developed from the derived Tafel Equation (Equation 1.34). In practice, an electrochemical reaction experiences a liming current density flow, J_l. This current density limit occurs when the electrochemical reaction is at the maximum rate possible for the given mass transfer conditions in which the reaction is taking place. When the limiting current density is achieved, the net rate of the reactions is completely governed by the rate at which species are brought to the electrocatalyst surface, ϕ_{MT}. Therefore, from Equation 1.27:

$$\phi = \phi_{MT} = \frac{J}{nF} \tag{1.35}$$

Mass transfer is the movement of species from one location in a solution to another. In particular for the application of this study, the movement of species to the three-phase boundary layer. There are three modes of mass transfer which include Migration, Diffusion, and Convection. Migration is the movement of a charged species under the influence of an electric field. Diffusion is the movement of a species under the influence of a concentration gradient. Finally, convection is the movement of species due to a flow of fluid. The effect of the limiting current density can be implemented into the Bulter-Volmer Equation by expressing the mass transfer rate in terms of the concentration of species. From the above equation an expression for the limiting current density can be developed.

$$\phi_{MT} = m_O[C_O^* - C_O(0,t)] \tag{1.36}$$

The above equation is an expression of the mass transfer rate in terms of the concentration of species and the mass transfer coefficient, m_O, which represents the volume flow rate per unit area. C_O^* is the concentration of species in the bulk solution and $C_O(0,t)$ represents the concentration of species on the electrocatalyst surface. Combining this equation with Equation 1.35 results in the following equation.

$$\frac{J}{nF} = m_O[C_O^* - C_O(0,t)] \tag{1.37}$$

The limiting current density occurs by definition when $C_O(0,t)$, the concentration of species of the electrocatalyst surface is zero, resulting in a maximum of the mass transfer rate, ϕ_{MT}. Under these conditions the above equation can be modified as the expression

for the limiting current density.

$$J_l = nFm_O C_O^* \tag{1.38}$$

These two equations can be combined to form an expression of the ratio of the concentration of species in the bulk solution to on the electrocatalyst surface. The equation below can be implemented into the Bulter-Volmer Equation to represent mass transfer effects.

$$\frac{C_O(0,t)}{C_O^*} = 1 - \frac{J}{J_l} \tag{1.39}$$

The Bulter-Volmer Equation, Equation 1.31, fit with the above express results in the following equation. This equation can be simplified to the Tafel Equation, in the same manner previously stated, shown in equation 1.41. Equation 1.42 is the resulting Tafel Equation rearranged to keep the current density, J, on the left hand side of the equation.

$$J = J_o \left(1 - \frac{J}{J_{lO}} exp\left[\frac{\alpha_O F(V_{op} - V_{min})}{RT}\right] - 1 - \frac{J}{J_{lR}} exp\left[\frac{\alpha_R F(V_{op} - V_{min})}{RT}\right]\right) \tag{1.40}$$

$$J = J_o \left(1 - \frac{J}{J_l} exp\left[\frac{(Vop - 1.23)\alpha F}{RT}\right]\right) \tag{1.41}$$

$$J = \frac{J_o \left(exp\left[\frac{(Vop-1.23)\alpha F}{RT}\right]\right)}{1 + \left(\frac{J_o}{J_l} exp\left[\frac{(Vop-1.23)\alpha F}{RT}\right]\right)} \tag{1.42}$$

This equation will be used to analyze the physical phenomena experimentally recorded, ultimately developing values of the exchange current density, J_o, the charge transfer coefficient, α, and the limiting current density, J_l for each test experiment. Quantifying these parameters provides a method of identifying and comparing the effects various electrolyzer

cell configurations and electrocatalyst materials have on the electrochemical behavior. The next section provides a review of the research that has been done on various electrocatalyst materials beginning with historical findings and concluding with specific results of nanostructured electrocatalyst.

1.4 Electrocatalyst Review

1.4.1 Historical Electrocatalyst Research

The first PEM electrolysis journal publication was presented in 1973 by Russell et al. from General Electric. This publication identified concepts that are only being realized as urgent engineering endeavors. Phrases mentioned, such as "future hydrogen economy", "hydrogen as energy storage", and "solar energy systems", now represent some of the more multi-faceted technological challenges yet to be fully realized. The publication also addressed the need to lower the cost of electrocatalyst materials, suggesting methods such as reducing catalyst loading and minimizing on the use of noble catalyst materials through the method of catalyst layering on various materials. Even earlier, in 1966, studies of the kinetics of the OER on Rh, Ir, and Pt-Rh alloys using a liquid electrolyte where being conducted, resulting in the ability to differentiate the alloys catalytic behavior from one another. The results showed Ir to be the most effective in comparison to Rh, Pt-Rh, and Pt [3].

A series of studies performed by Burke and Moynihan during the 1970's contributed to valuable discoveries in electrocatalyst materials for the OER. Each part of the study provided some insight into how electrocatalyst contribute to the OER. They found an OER over Ru caused vigorous corrosion under strongly oxidizing conditions with a variety of oxidation states. It was also determined that d-band vacancies play an essential role in oxygen

chemisorption, the concentration of such vacancies in Ru was found to be too great for the OER [23]. Later work accounted for the metallic conductivity of RuO_2, identifying the ability of Ru to form oxide bridges with two three-center molecular orbital bonds as the cause. A reduction of these oxide bridges , which are also involved in the incorporation of Ru in the oxide films on Pt, would lead to a loss of Ru and a decrease in catalytic activity [24]. The second series of Burke and Moynihan's work led to a greater understanding of the OER. They determined that OH radicals never covered a large surface of the electrocatalyst at any one time while the conversion to an oxide film occurred. They assumed the OER was governed by similar mechanisms [25].

In the years following, research has been focused on the discovery of an electrocatalyst which can make up for the slow nature of the OER while enduring the highly anodic conditions of the anode. Activities of various elements have been characterized for the OER though it has been shown that the oxides of these elemental catalyst seem to have a dominate factor in affecting electrocatalytic properties [26]. RuO_2 has been known to exhibit overpotentials much lower than other material tested for the OER [27, 28]. As an example, the overvoltage for the OER is much lower with RuO_2 or Ru than with Pt [27].

1.4.2 Current Electrocatalyst Research

Pt has been identified as the optimal electrocatalytic material for the HRR [27, 29]. A material of the same caliber has yet to be determined for the oxygen evolution reaction and thus the search for an active, stable, and inexpensive anode electrocatalyst has been pursued by many [30]. Detailed modeling studies have been performed utilizing thermochemical density functional theory (DFT) of the OER. These studies have identified the binding energy of a surface oxygen species to be the activity-controlling parameter of the reaction,

yielding a volcano type activity plot, with Ru and Ir oxide near the top [31]. Both of these materials have emerged as the most promising catalyst candidates for the OER. IrO_2 is currently recognized as the state-of-the-art electrocatalyst material for the OER in water electrolysis. Although RuO_2 has shown to be the more active electrocatalyst material, it is associated with instability issues such as corrosion [32]. Current research has been focused on modifying IrO_2 catalyst in a variety of ways to increase the electrocatalytic activity and durability. Some studies have explored mixing IrO_2 with 'dilutants' to produce a cheaper and more durable material [33], though this often leads to poor electrical conductivity of the electrode. Others create mixtures such as SnO_2-IrO_2-Ta_2O_5 in order to expand the surface area, improve the electronic conductivity, increase the charge storage capacitance and promote the surface enrichment of iridium [34]. The results of this particular study showed that the electrocatalytic properties of IrO_2 are still prevalent at low concentrations, though the specific samples used could not be utilized in a membrane electrode assembly (MEA) or catalyst coated membrane because of the impermeability of the solid catalyst plates [34]. The most evident conclusion drawn from electrocatalyst research is that the ideal catalyst material must provide, high electron conductivity, high mass transport and high durability, while material loading is minimized [3].

1.5 RuO_2 Nanorods

The focus of this research is to operate a PEM water electrolyzer with the aid of a nanostructure decorated electrode surface, specifically, implementing RuO_2 nanorods as an anode catalyst material. The use of RuO_2 as an OER aiding electrocatalyst has been studied extensively. Initially RuO_2 films displayed the lowest overpotential for the OER ever observed [35]. The use of RuO_2 as an electrode material was pursued diligently as a result. In 1970 Trasatti and Buzzanca published research on the solid state structure and electrochemical behaviors of RuO_2 in which they presented the advantage of the low temperature

decomposition of $RuCl_3$ in air to create thin film samples [27]. More recently RuO_2 has been explored for use as an electrode for the OER in aqueous environments. A specific study recently published in the Electrochimica Acta compared the electrocatalytic activities of amorphous RuO_2 to that of rutile crystalline RuO_2. This study suggested the structural flexibility of amorphous RuO_2 films attributed to the enhanced electrocatalytic behavior when compared to the crystalline RuO_2 [36].

The implementation of nanoparticles as electrocatalyst for the OER has also been a topic of recent interest. Since the cost of both IrO_2 and RuO_2 are high, there is an eagerness to advance nanoparticles with high surface area-to-mass ratios [37]. There have been claims that rutile RuO_2 exhibits greater electrocatalytic activity than rutile IrO_2 [38]. The same has been shown while comparing the two materials synthesized as nanoparticles in both acid and alkaline environments . In fact there is evidence that oxide nanoparticles exhibit higher stability under OER conditions than commercial Ru/C and Ir/C catalyst [37]. The instability of carbon supported Ru and Pt nanoparticles was discussed by Reier et al. in 2012 when comparing nanoparticle and bulk material electrocatalyst for the OER. The results showed Ru/C nanoparticles suffered from strong corrosion at OER potentials. The Pt/C nanoparticles exhibited lower OER activity than bulk Pt ultimately becoming inactive. The highlight of this study was the comparable OER activity and durability for Ir/C nanoparticles and bulk material [39].

Less has been determined for the electrocatalytic behavior of nanostructures. Certain oxide nanoparticles will form into sea urchin shaped nanorods which have potential to increase electrocatalyst surface area and provide enhance electric field effects. This concept has been explored for both the ORR and OER, focusing on an electrocatalyst for a Lithium-Oxygen battery. In the study, Jang et al. synthesized α-MnO_2/RuO_2 nanorods

and characterized the performance as an electrocatalyst for both the ORR and OER. A bifunctional catalyst for the air cathode of a lithium-oxygen battery was created by mixing α MnO_2, the most active material for the ORR, and RuO_2, the most active material for the OER. The results compared the nanorods to commercial Pt/C electrocatalyst for both ORR and OER. The performance of the nanorods were comparable to the Pt/C for the ORR, while lower onset potential and higher limiting current was displayed by the nanorods for the OER [40]. Although these results don't directly relate to the use of nanostructure electrocatalyst for PEM electrolysis, they do provide insight to the enhanced electrocatalytic activity for the OER. This supports the ability of nanostructure materials to overcome limitations of present commercial electrocatalyst by providing suitable, sustainable and cheap solutions for the technological development of electrocatalytic water electrolysis.

The electrocatalytic material which is the focus of the present study is rutile crystalline RuO_2 nanorods. There is evidence that this material may be beneficial for the OER because it provides a large surface area [41]. Figure 1.7 is a scanning electron microscope (SEM) image of the RuO_2 nanorod decorated Telpro mixed metal oxide ribbon mesh anode surface. Appendix A includes multiple images of each of the samples tested. The sharp geometric features of this engineered electrode material also have the ability to produce a high electric field at the surface, which in theory will lower the required activation energy of the electrochemical reaction as previously stated.

1.5.1 Surface Area

As can be seen in Figure 1.7, the interfacial area of the nanostructure coated electrode surface is composed of a field of RuO_2 nanorods. The nanorods can be grown longer than 1 μm and are controllably made 10 to 1000 nm wide in the lateral dimension [42]. Because

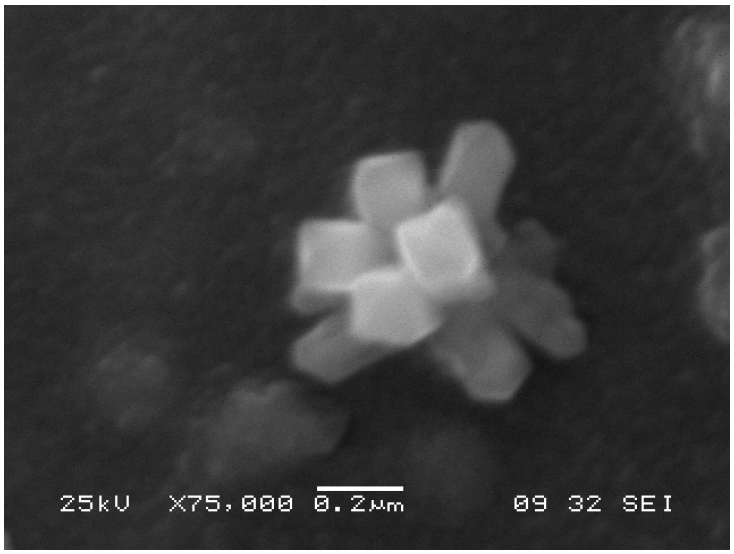

Figure 1.7: SEM Image of RuO_2 Nanorods

RuO_2 is an electrical conductor, it can be treated as part of the electrode surface. The increase in interfacial area has been measured in previous experiments to be on the order of a factor of 10. This increase in surface area also increases the amount of possible area available for the three-phase boundary layer required for the electrochemical reaction on the electrocatalyst layer of the MEA. [43]

1.5.2 Enhanced Electrical Field

The shape of an individual nanorod is rectangular with sharp edges. Figure 1.7 shows the pyramid shape ends of the nanorods. When electrically biased, a high field region forms around the exterior of the rectangular nanorods. The magnitude of this electric field is inversely proportional to the size of the nanostructure, and therefore a high field strength is expected around the exterior vicinity of the nanostructure. Since the nanorods will be facing the high proton conductive membrane and negatively biased cathode electrode layer, an electrical field will be produced around the positively charged nanorods due to the nega-

tively charged surrounding area. As mentioned earlier this enhanced field effect is expected to decrease the reaction overpotential resulting in enhanced electrocatalytic behavior. The GDL will promote a solid-gas interfacial environment as apposed to a solid-liquid interface between the nanorods and the water reactant. This is expected to alter the double layer effect previously mentioned. Figure 1.8 shows a sketch of the expected electric field around the nanorod tip.

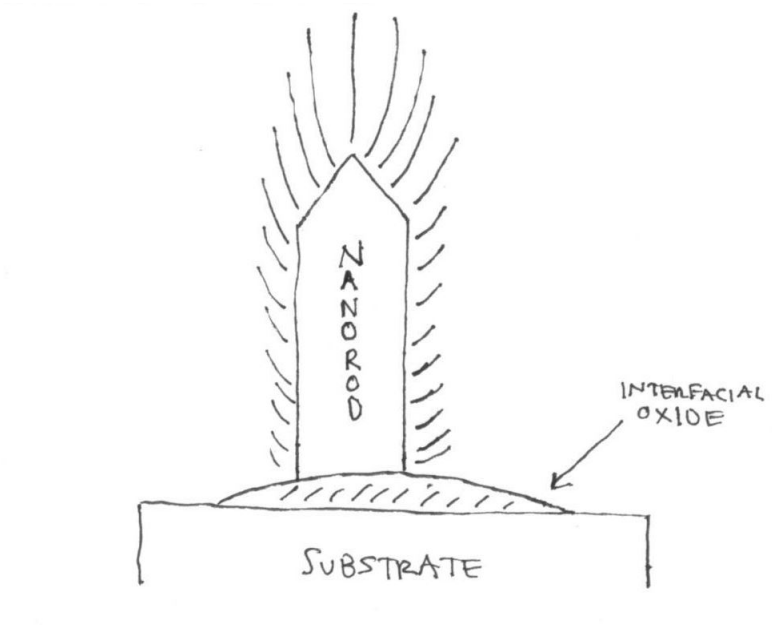

Figure 1.8: Increase electric field around tip of nanorod.

1.6 Experimental Practices and Procedures

A mixture of experimental analysis and literature review led to the laboratory experiment design that was implemented for this study. A fine balance between these two modes of insight exposure was required when developing the final design. While reading about the

functional requirements of each system component provided information on the specific component, the experimental evidence exposed the functional relationships between components. This method of design ultimately led to a greater understanding of the PEM water electrolysis system while creating some limitations on the final system design which will be explained in the next chapter.

Chapter 2

Materials and Methods

2.1 PEM Water Electrolysis system

The majority of effort and time was dedicated to the design of the PEM water electrolysis laboratory experiment. Determining the appropriate location of the electrocatalyst in the PEM electrolyzer cell as well as fine tuning the MEA anode environment proved to require extensive experimental analysis. The PEM electrolyzer system is a delicately constructed stack of unique material layers which require specific environments in order to provide various electrical, chemical and mechanical modes of transport for participating reactants. It was experimentally discovered that an imbalance experienced by any layer of the PEM electrolyzer cell would contribute to non-ideal operation. This chapter will elaborate on the laboratory design process while discussing operational optimization findings, developed through both experimental analysis and research of documented procedures.

Each component of the PEM water electroylzer posses potential changes to their constitution, which require a fine balance in enhancing performance. The same can be said about the electroylzer system as a whole; a change in layer position, material, or hydration can result in varied operational behavior. Changes to individual components of the system

affect the performance of that component specially, which in turn affect the operational relationships between the different components of the whole system. The nature of this system behavior required fine attention to detail when making system modifications. The effect of making changes to different components of the electrolyzer cell has to be considered in order to maintain optimal performance.

The PEM water electrolysis system designed for this study is shown in Figure 2.1. The overall system consists of a PEM water electrolyzer cell, a water pump, a power supply, and two digital multimeter (DMM). The following sections will describe each of these system components and the procedures used to characterize the various anode electrocatalyst. The electrolyzer cell was designed to compare anode electrocatalyst materials and thus there was a focus on maintaining a constant cathode environment. When describing the PEM water electrolyzer cell, the cathode component will be treated first, followed by the anode component.

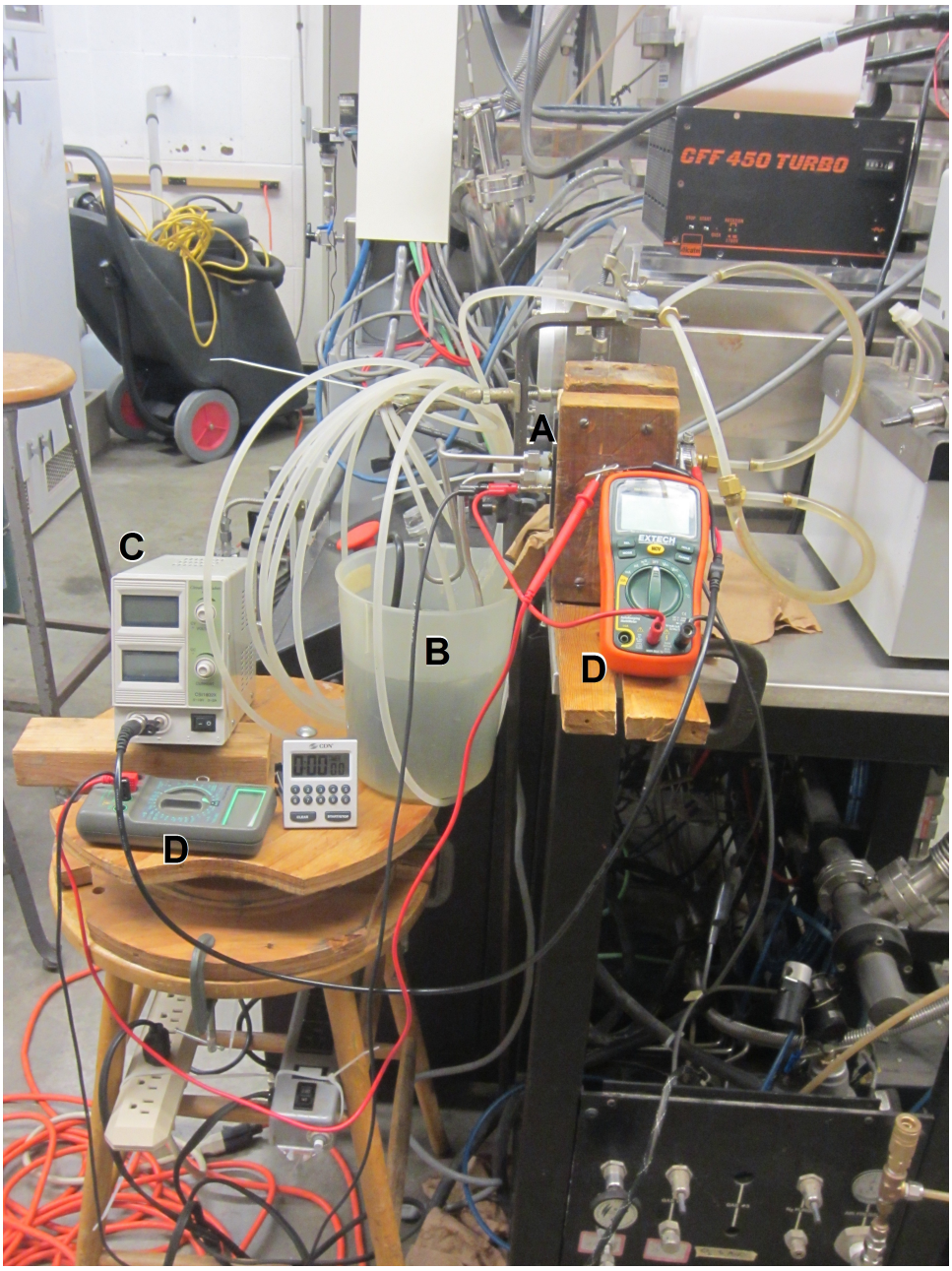

Figure 2.1: PEM Water Electrolysis System
A. PEM Electrolyzer Cell B. Water Supply Pump C. Power Supply D. Digital Multimeter

2.2 External Components

The system components which surround the PEM water electrolyzer cell will be described in this section. They include the water pump, power supply, two digital multimeters and the system structure. PEM water electrolysis requires two inputs, water and a voltage potential. DMMs are used to measure applied voltage to the cell as well as current provided. The electrolyzer cell is set into a wooden stand while a metal arm is used to suspend the water feed tubing. A detailed description of each of these components follows.

2.2.1 Water Supply

Water is supplied to both the bipolar plates using a 19 W Power Head King-225 water pump rated at 1500 $\frac{L}{Hr}$ maximum flow rate. The water pump is positioned next to the PEM water electrolyzer cell in a 2000 mL plastic Nalgene beaker. Water is pumped to the electrolyzer cell through a flexible tube, which is coiled to achieve a total flow rate of 250 $\frac{mL}{min}$. A Swagelok T fitting is used to split the water feed to the cathode and anode bipolar plates resulting in a 125 $\frac{mL}{min}$ supply rate to each side. Plastic Swagelok fittings are used to connect the outputs of the bipolar plates to stainless steel, u-shaped piping. This is to ensure there is no electrical contact between the electrolyzer cell and the water feed plumbing. These u-shaped pipes purge excess water out of the electrolyzer cell back into the initial Nalgene beaker creating a closed loop water supply system. Appendix B.1 contains a sketch of the water supply system.

2.2.2 Power Supply and Digital Multimeters

A voltage potential is provided to the PEM water electrolyzer cell by a CSI1802X power supply from CircuitSpecialist.com. This power supply is rated to 18 volts and 2 amperes maximum. Negative potential is applied to the cathode bipolar plate using the voltage measurement banana plug located above the outlet. Positive potential is applied to the anode bipolar plate via a screw clamp which is wrapped around the metal swagedlok inlet. Figures 2.2 and 2.3 show these connections. To ensure constant voltage control operation, the current control knob is set to it's maximum position for all data acquisition.

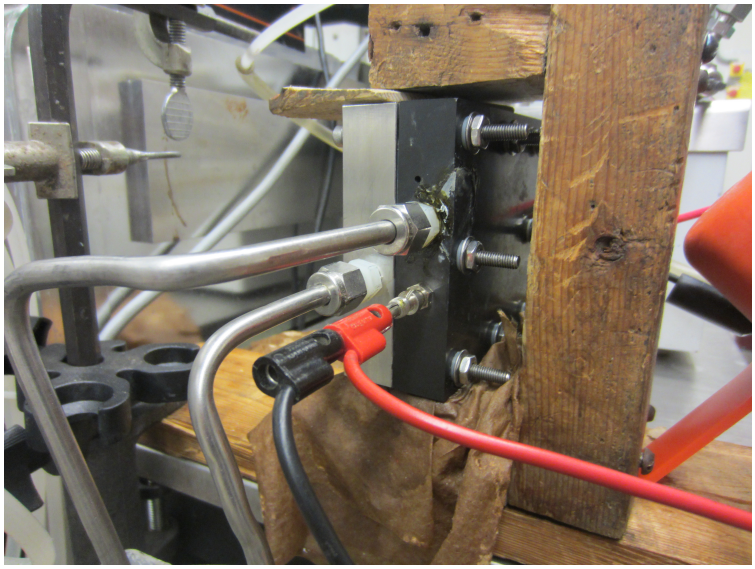

Figure 2.2: Cathode Voltage Measurement Connection

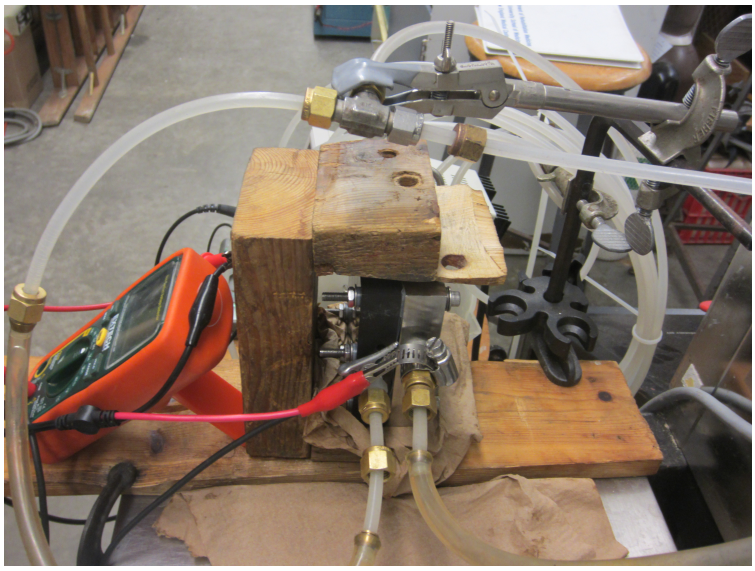

Figure 2.3: Anode Voltage Measurement Connection

An Extech EX330 digital multimeter(DMM) is used to measure the applied voltage to the electrolyzer cell while in operation. This DMM is also used while assembling the cell to measure the resistance between the bipolar plates. A WaveTek DM10XL digital multimeter is used to measure the current applied to the electrolyzer cell while in operation. Each DMM is set to measure to the nearest hundredth. An electric circuit diagram of the PEM water electrolysis system is included in Appendix B.2 .

2.2.3 System Structure

A wooden stand was self assembled using a plank of dimensions $9cm$ wide, $1.5cm$ thick, and $42cm$ long, a $15.5cm$ long, $8.5cm$ wide, and $3.5cm$ thick block and two $5.5cm$ by $5.5cm$ by $3cm$ wooden pieces. This stand is secured to a metal laboratory table using two C-clamps, one of which holds a metal arm. The arm extends over the wooden stand, forming an L-shape, while holding the plastic tubing which feeds the water to the electrolyzer cell. Both

the water pump and power supply are positioned next to the metal laboratory table on a laboratory bench which also holds a 15 Amp max power strip.

2.3 PEM Electrolyzer Cell

2.3.1 The Bipolar Plates

The major function of the bipolar plates is to provide efficient modes of mass transport for reactants and products, in the case of water electrolysis the reactants are $H_2O(g)$ and the products are $H_2(g)$, and $O_2(g)$. They also aid in the collection of current, maintaining thermal stability, and providing balance of fuel supply. Bipolar plates are commonly made of metals, metal alloys or graphite. The material choice focuses on durability, cost, conductivity, chemical compatibility, and the ability to diffuse gas [44].

A demonstration fuel cell was purchased from the FuelCellStore and modified to function as the PEM water electrolyzer cell. The modified cell consists of the original graphite bipolar plate functioning as the cathode while a self fabricated stainless steel bipolar plate is used as the anode. The graphite cathode bipolar plate has a serpentine gas flow field ($5.175cm^2$ surface area, $0.1cm$ deep), grooved into the center of the side that faces the MEA. The stainless steel anode has an open gas flow field ($4.95cm^2$ surface area, $0.2cm$ deep) which provides space to alter the anode side of the cell.

The principle action of the bipolar plates, to distribute reactants, is accomplished by the race track like flow field openings in the center of each plate. The most common flow field designs, parallel and serpentine, are shown in Figure 2.4. The design of these flow fields govern the distribution and flow rates of the reactants. Parallel flow channels are

consistently used because they provide a uniform pressure drop across the entire flow field. The pressure drop across the flow field causes the reactants to flow which the performance of the electrolyzer is heavily dependent on. In fact, any inconsistency in flow rate can lead to an impact on the performance of the entire system. The flow rate of reactants from the bipolar plate is proportional to the current density [45].

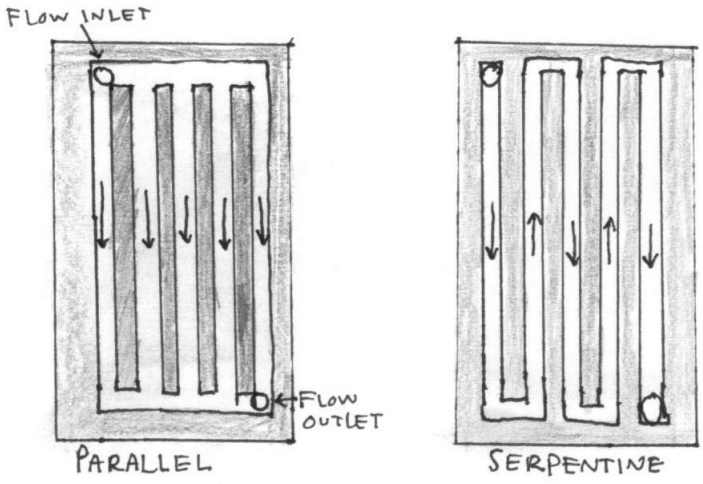

Figure 2.4: Common Flow Field Designs

A recent study was able to explore the impact of flow field geometry and design using computational fluid dynamic modeling and simulation. The highlights of this research included the understanding of pressure drop across the flow field in relation to the channel width. As the channel to land ratio of the flow field increased, the pressure drop across the flow field decreased. The lower the pressure drop, the lower the losses due to friction and the better the mass flow rates of the reactants [46]. Ultimately this would insist that to minimize pressure drop across the flow field requires maximizing the channel to land ratio. This would require the land width to approach zero, resulting in an open flow field with no channels. In practice, this would cause uneven distribution of reactants as well as

poor current conductivity of the bipolar plate. A delicate balance is required between the channel to land ratio and pressure drop.

Initially, the plan was to place the various electrocatalyst samples into the open anode flow field. Although this provided optimal electrical contact between the electrode and bipolar plate, there was no room for a GDL and thus flooding of the electrode occurred. Also the physical distance between the electrode and Nafion membrane proved to be too great and limited the mass transport of the reactants.

Two plastic gaskets from the demonstration fuel cell, with a $6.45cm^2$ window allowing membrane exposure, are put in between the bipolar plates and GDL to ensure a proper gas tight seal. Stainless steel current distributors were initially fitted around the window of the gasket of the anode to provide ample contact between the GDL and stainless steel end plate. Two $1mm \times 2mm$ sheets of stainless steel were folded about the window of the anode gasket, one on each side of the window, providing $2mm^2$ total contact area between the GDL and the anode bipolar plate. These current collectors were effective but ultimately were not used in the final design. Figure 2.5 shows these current collectors positioned around the gasket window.

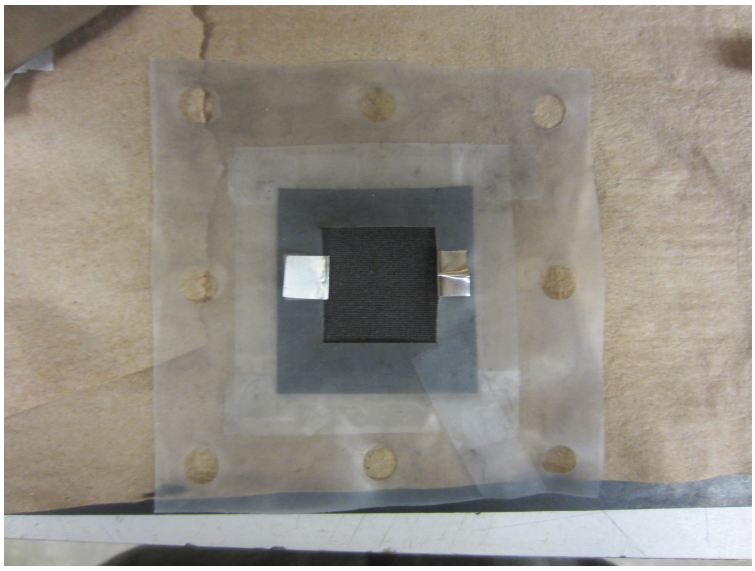

Figure 2.5: Stainless Steel Current Collectors Positioned Around Anode Gasket Window

The open anode flow field caused uneven distribution of the water across the GDL as well as poor pressure control. Proper pressure and physical support are required when fitting the MMO ribbon mesh Ti anode electrocatalyst structure into the electrolyzer cell in order to avoid physical damage to the Nafion membrane and GDL caused by excess pressure pushing these materials together. In order to accommodate for this, a Ti ribbon mesh anode is fit into the anode flow field. This provides the physical support and proper pressure drop across the field to eliminate the physical damage caused by the anode electrocatalyst structure. The flow field fitting also provides proper conductivity between the bipolar plate and GDL, and thus the stainless steel current collectors became obsolete and were removed to avoid possible corrosion of the material. The serpentine flow field of the cathode bipolar plate provides sufficient conductivity to the GDL so no further modification is required. Figures 2.6 - 2.8 show the various configurations of the anode flow field and the face of the cathode flow field.

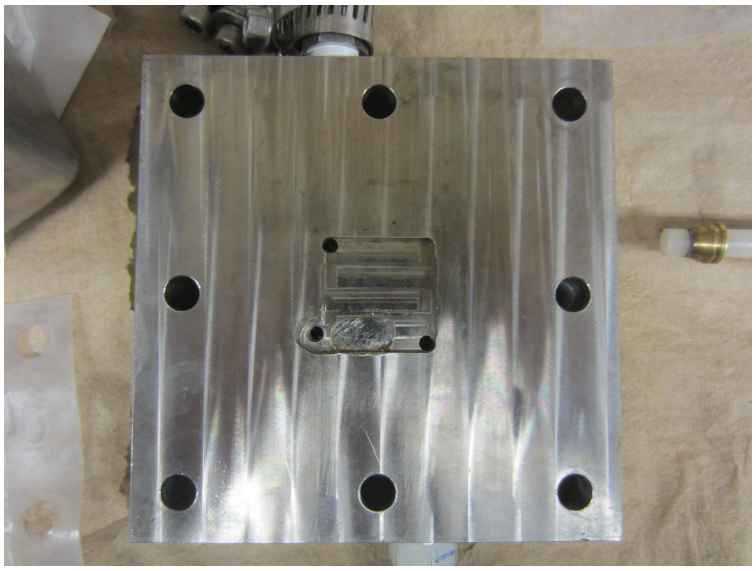

Figure 2.6: Stainless Steel Anode Bipolar Plate and Open Flow Field

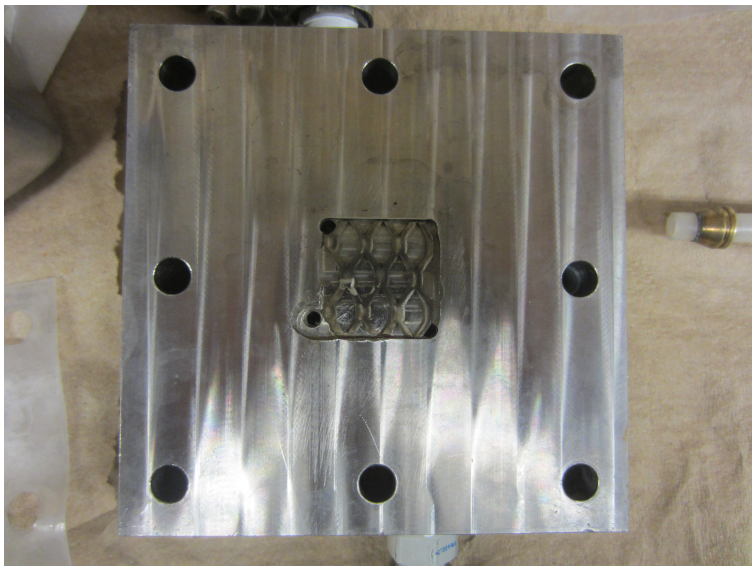

Figure 2.7: Anode Flow Field with Ti Ribbon Mesh Fitting

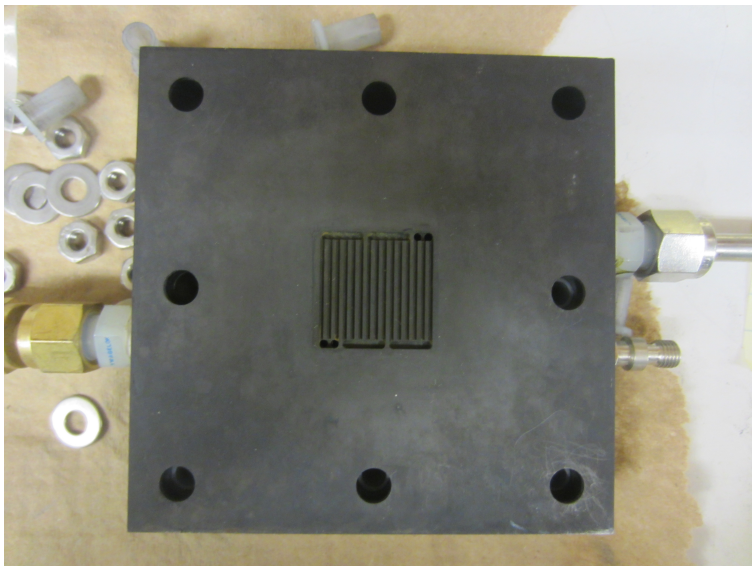

Figure 2.8: Graphite Cathode Bipolar Plate and Serpentine Flow Field

2.3.2 The Gas Diffusion Layer (GDL)

As previously stated, the GDL provides additional modes of mass transport for the reactants as well as acting as a conductive link between the electrocatalyst and the bipolar plate. What differentiates these responsibilities from those of the bipolar plates is the GDL controls the balance of liquid and gaseous H_2O seen by the electrocatalyst surface and Nafion membrane. Characteristics of ideal GDL materials include excellent electrical conductivity, optimal porosity, and proficient wetting and de-wetting properties [47]. The GDL protects the electrocatalyst surface from flooding caused by liquid H_2O while providing sufficient gaseous H_2O for the electrochemical reactions to occur as well as hydrating the Nafion membrane for efficient proton transfer. The GDL ultimately acts as the operator of water electrolysis system by controlling the environmental variables of the system in order to optimize the overall performance.

The GDL of PEM fuel cells are generally made up of woven carbon fibers in the form of

cloth or paper. Carbon cloth has proven to provide support to the MEA and is commonly included as a layer of 5-layer MEAs. There is evidence of carbon based materials oxidizing under OER environments and thus carbon cloth GDLs are not suggested for use on the anode side of electrolyzer cells. The oxidized carbon converts to CO_2, consuming the GDL and eventually leading to poor conductivity. Thin Ti screens coated with a very thin layer of Pt have been suggested as efficient replacements for carbon based GDLs. The Pt layer increases the life time of the Ti while increasing the conductivity [48].

The oxidation of the GDL was experienced experimentally. Numerous water electrolysis trials with the use of carbon cloth GDL on the anode side of the electrolyzer cell resulted in discoloration of the GDL and a slight decrease in performance. This event only occurred over multiple uses of the same GDL with minimal effects in relation to other experimental variables. Therefore the use of carbon cloth GDLs was continued with the condition and duration of implementation closely monitored. Replacement of the anode GDL was performed before each important experiment was conducted.

The cathode GDL used in all experiments is included in the membrane electrode assembly and thus will be mentioned when describing the various MEAs tested. The anode GDL consists of woven carbon cloth purchased from FuelCellEct. A $4.2cm$ by $4.4cm$ piece is cut and taped on the anode gasket using masking tape. This helps in the assembly of the cell to ensure the GDL is set evenly. Figure 2.9 shows the GDL through the window of the anode gasket which faces the anode flow field.

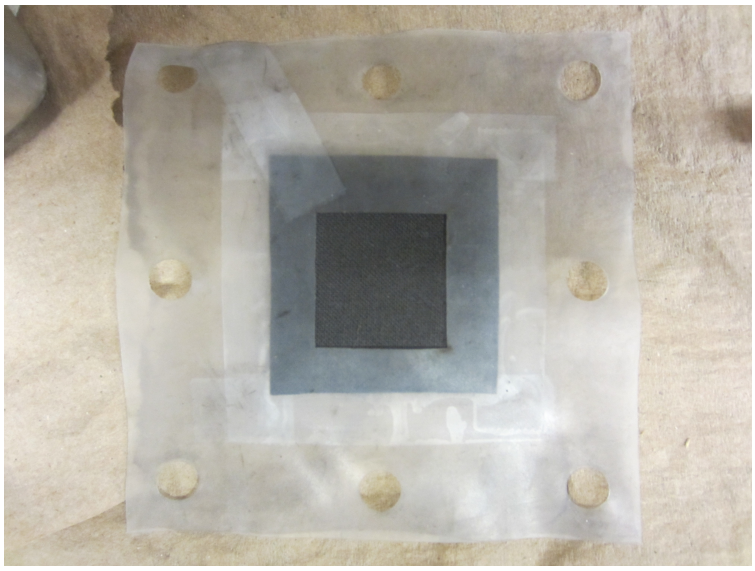

Figure 2.9: Anode GDL and Gasket

2.3.3 The Membrane Electrode Assembly (MEA)

The heart of the PEM water electrolysis system is the MEA. The location of the electrochemical reactions, the MEA consist of numerous components each with their own potential for optimization. Of the many components that make up a PEM water electrolyzer cell, the MEA represents the layer in which balance is of most importance. Though commonly consisting of 5 layer, the model of MEA discussed in this section only acknowledges 3 layers, the Nafion membrane and each electrode (cathode and anode), since the outer GDL has already been treated. These layers have also been previously reviewed in an earlier chapter and thus this discussion will focus on the experimental discoveries related to these layers and the resulting MEAs used in the experiments.

The order in which each layer is stacked in a MEA was determined to be essential to proper operation. As Figure 2.10 shows, the MEA consists of the membrane center, commonly loaded with the electrocatalytic material , to ensure intimate contact, which is then

covered with a carbon cloth GDL. In order to study the affect of the RuO_2 nanorods as an electrocatalyst, a conventional MEA needed to be disassembled. There are multiple MEAs used in this study in order to obtain the data required to fully compare the different electrocatalyst. The cathode side of the MEA remained constant throughout the study and thus will be explained first, followed by the variations of the anode side of the MEA. All MEAs used in this study are cathode loaded with 4 $\frac{mg}{cm^2}$ PtB and covered with a carbon cloth GDL. The membrane used for all MEAs is Nafion 115 which is 127μm thick.

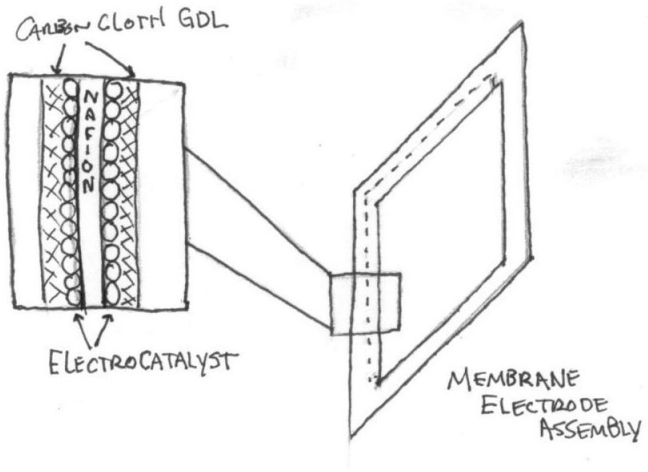

Figure 2.10: Layers of the Membrane Electrode Assembly

The MEAs differ in anode catalyst loading and location of the GDL. The various catalyst loading includes no loading and loading of 3 $\frac{mg}{cm^2}$ $IrRuO_2$. The location of the GDL varies between being included in the membrane electrode assembly as well as being separated as it's own layer.

2.3.4 Anode Electrode

The electrocatalyst material varies between various tests. Three samples of the Telpro MMO ribbon mesh anode are prepared and tested for comparison. Each piece is cut into a $2.2cm$ by $2.1cm$ sample and the edges are sanded to eliminate possible damage to the MEA or GDL. One sample is left alone as the Telpro MMO ribbon mesh anode which is covered with Ir/Ta. The MMO is stripped from another sample, creating a Ti ribbon mesh anode. The final sample consists of a Telpro MMO ribbon mesh anode decorated with RuO_2 nanorods. The nanorods were deposited under very specific process conditions of; substrate temperature, gas composition, and sputter target power in a reactive sputtering process which supported a self-assembly mechanism that has been discussed more fully in a previous publication [41].

The optimal electrode placement is tested using the Telpro MMO ribbon mesh anode electrode. Initially, the maximum distance between the electrode and Nafion membrane was explored by placing the electrode in various locations and placing a catalyst guard between the Nafion membrane and electrode. This catalyst guard, shown in Appendix E, was self designed using SolidWorks and fabricated using a 3-d printer. The guard was designed to protect the electrocatalyst material while allowing for reactant flow and no electrical conductivity between the Nafion membrane and electrode. The following Figure 2.11 shows the various anode electrodes which were used in these tests.

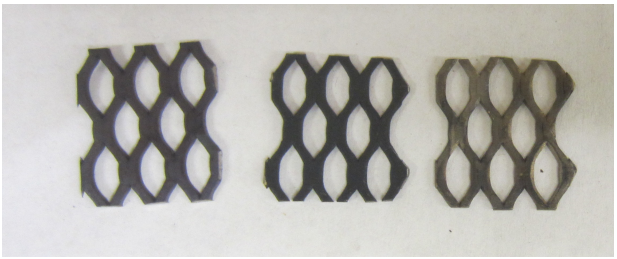

Figure 2.11: Various Anode Electrodes Compared
From left to right: RuO_2 nanorod decorated MMO ribbon mesh anode, Ir/Ta MMO ribbon mesh anode, and Ti ribbon mesh anode.

2.4 Test Procedure

The internal design and construction of the PEM electrolyzer cell was a significant portion of the overall experimental process while the other aspects included electrolysis activity measurement, cell assembly, and modes of water feed. These design aspects were also developed through both experimental and literature analysis. Fortunately, single cell test protocols and cell assembly procedures are well documented for PEM fuel cell systems. Application of these documented methods were adapted to the PEM water electrolysis system with little implications.

The test procedure consists of three main steps, PEM water electrolysis system assembly, preconditioning the system, and conducting a set of measurements that create a polarization curve of the steady-state current density vs. applied voltage of the cell. These steps are described in more detail in the following sections.

2.4.1 Assembly

The assembly of the PEM water electrolysis system consists of three parts. Assembling the external components which were identified in an earlier section, assembling the PEM water electrolyzer cell, and hooking the electrolyzer cell up to the external system components. In practice, the assembly of the external components is done once and maintained throughout the period of testing. This section will explain the initial assembly from ground zero and also discuss the required maintenance. Step by step images of electrolyzer cell assembly are in Appendix C.

The wooden stand described earlier is secured to a metal laboratory table using two C-clamps. One of the two C-clamps also holds a metal arm which extends over the wooden stand as shown in Figure 2.1. A laboratory bench is set next to the laboratory table and fitted with a 15 A power supply. This is the extent of the structural system assembly. A water pump is fitted with a plastic tubing, which is coiled to provide a flow rate of $250\frac{mL}{min}$. Proper water feed is required to ensure proper pressure as well as the initial flow rate of water into the cell. Previous studies on electrolyzer cell performance related to flow rates show an optimal flow rate of $20\frac{mL}{min}$ to $110\frac{mL}{min}$ [3, 49]. The coiled tubing is suspended with a metal arm above the wooden stand, where it is split in two by a Swagelok T fitting. At either end of the T fitting, plastic tubing is attached. The water pump is submerged into a 2000 mL Nalgene beaker, filled with 1600 mL of water. This beaker is place on the laboratory bench closest to the edge of the laboratory table. The water pump is plugged into a power strip which is switched on for operation. The power supply is set to the left of the water supply on the laboratory bench and plugged into the same power strip. The DMM is set in front of the power supply and set to measure the applied current. Once these aspects of the system are prepared the external components are assembled.

The assembly of the PEM water electrolyzer cell involves stacking the different material layers in the cell. First the Swagelok fittings are installed to both inlets and outlets of the bipolar plates ensuring the outlets are plastic and the anode inlet has a screw clamp fastened tightly around it. The stainless steel pipes are then connected to the outlet fittings and tightened. The stainless steel anode bipolar plate is fitted with the bolts, washers and plastic bolt fittings so that the hex heads of the bolts face down and the threaded ends of the bolts go through the bipolar plate. The Ti ribbon mesh anode flow field fixture then is placed in the anode flow field. Next the GDL layer fitted gasket is placed so each bolt goes through it's perspective hole and that the carbon weave faces the anode flow field. The anode electrode sample is placed on top of the GDL, located in the flow field area, with the electrocatalyst surface facing up. The MEA is dipped in water and then placed, anode side face down on the stack. The MEA will begin to curl and physically deform once it is wet, so it helps to hold the corners down while placing the next layer, the cathode gasket. This gasket is laid in a similar manner as the anode gasket, the difference is there is no GDL attached. The final layer placed is the cathode bipolar plate, orientated so the inlet and outlet match that of the anode bipolar plate and fitted with bolt fittings, washers and nuts. A weight of some sort can be placed in the middle of the cathode bipolar plate to ensure the MEA does not shift while the bolts are tightened.

The bolts are tightened in the pattern shown in Figure 2.12. They are initially finger tightened with the electrolyzer cell still orientated as when layering the stack. Then the weight is removed, the cell is set upright, and the bolts are finger tightened in the same pattern until secure. While tightening the bolts it is important to use the DMM to measure the resistance between the cathode and anode bipolar plate. If the resistance is zero then there is an issue with the assembly and the stack must be reassembled. If resistance of approximately $10k - 100k$ ohms is measured between the bipolar plates, and the bolts are

fully finger tightened, then the PEM water electrolyzer cell is assembled and ready to be connected to the external system components.

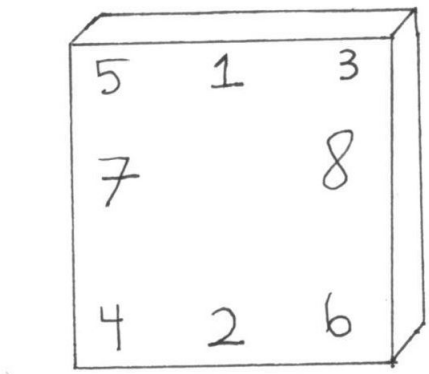

Figure 2.12: Tightening Pattern of Electrolyzer Cell Bolts

The cell is first set into the wooden stand so that outlet tubing sits above the water supply beaker. A small wooden wedge is used to secure the electrolyzer cell into the wooden stand. The inlet fittings are connected to the plastic tubing and the cell resistance is measured for ensure nothing has changed while setting the electrolyzer cell. Once set, the water pump is activated by turning the power strip on. Once the water begins to flow any air bubbles in the plastic tubing are removed and the cell is checked for leaks. Upon successful assembly, water should flow through the electrolyzer cell with minimal leakage creating a closed loop water supply system. This system only requires replenishing the water in the Nalgene beaker which is lost due to evaporation or system leakage.

2.4.2 Preconditioning

Once the PEM water electrolyzer cell is connected to the external system components, and the closed loop water supply is running with minimal leakage, the electrolyzer cell needs to be preconditioned. As stated previously, hydration of the Nafion membrane is vital to achieving optimal proton transfer, and ultimately, the resulting amount of hydrogen gas produced. In order to ensure proper hydration of the Nafion membrane, the electrolyzer cell is supplied with water for at least 1 hour before any voltage is applied. The US Fuel Cell Council (USFCC) protocol insists on a 30 minute hydration period [50], though a period of 1 hour was allotted for this experiment to obtain consistent, repeatable data. After this 1 hour period had passed, the resistance of the electrolyzer cell is checked to ensure the conductivity between the bipolar plates is still not a short or open circuit.

An additional voltage preconditioning period follows by connecting the power supply to the electrolyzer cell, setting the DMMs to measure current passing through the cell and the voltage potential between the cells, and applying a voltage of around 2.5V. The USFCC protocol, which calls for a 1 hour period of constant applied voltage at 1.8V [50], was used as a bench mark to develop a 1 hour at 2.5V precondition process which provides consistent operation. These preconditioning periods provide time for the electrolyzer cell to achieve steady state operation.

2.4.3 Cell Polarization

There are a variety of experimental methods used to determine the activity of water electrolysis. Studies previously discussed utilized different methods including cyclic voltammetry, polarization curves, and Nyquist plots [51]. The method used herein, operates on

the relationship between hydrogen production and measured electrical current between two electrodes under water electrolysis conditions. The quantitative concepts of electrolysis were developed by Michael Faraday in 1834 and published as Faraday's laws of electrolysis [7]. The first law states that the mass of the products produced on the electrodes is proportional to the value of current supplied to the electrolysis cell. This is expressed mathematically in the following equation.

$$m = \frac{QM}{Fz} \tag{2.1}$$

m is the mass of the product produced at the electrode in grams, Q is the total electric charge passed through the solution in coulombs, M is the molar mass of the solution in grams per mole, F is the Faraday Constant (96485 C mol^{-1}), and z is the valency number of ions of the solution or the number of electrons transferred per ion [52]. Applying this equation to the production of hydrogen via water electrolysis leads to the following derived relationship:

$$Q(c) = I(A)t(sec)$$

For hydrogen gas:

$$M = 2.01588(\tfrac{g}{mol})$$

$$Z = 2(\tfrac{e^-}{mol})$$

Equation 2.1 becomes the current-time dependent equation for the mass of hydrogen gas produced in grams :

$$m = It\phi \tag{2.2}$$

where ϕ, the conversion constant relating the grams of hydrogen gas to coulomb charge, is expressed as $\phi = \frac{M}{Fz} = 1.045 \times 10^{-5}(g)$.

It is Faraday's laws of electrolysis which provide the quantification required to compare various electrocatalyst materials based of measured electrical current. Therefore, the cell

polarization test of the PEM water electrolyzer is used as the primary method of performance comparison.

At the end of the 2 hour preconditioning period of the electrolyzer cell, an initial reading is taken and then the voltage is set to 2.5V. The voltage sweep performed is a 0.2 V initial decrease from 2.5V to 2.1V and then a 0.1V decrease from 2.1V to 0.8V. A final reading is taken at 0.6V. Sixty seconds are allotted between each voltage increment to allow for steady state condition to exist. If current is still flowing when 0.6V is applied, an additional 0.2V drop is made until the current reads 0A. The power supply is then turned off and disconnected, as is the water supply, and the electrolyzer cell is removed from the wooden stand, opened, loosening each bolt in reverse assembly order, and disassembled layer by layer, noting any physical changes that could have occurred during the operation of the cell. Appendix D is of a sample data sheet used to record the resulting data produced by this experiment.

An Excel spreadsheet was created to process the collected data. Equation 2.2 was used to determine the amount of hydrogen produced. Polarization plots were produced by plotting the applied voltage (V) vs. the measured current density ($\frac{mA}{cm^2}$). Current density is calculated by dividing the measured current by the total projected surface area. This active area is determined based on the dimension of the anode electrode as it is often the smallest active area component in comparison to the exposed area of the flow field and Nafion membrane. These plots were compared to published results of similar experiments to ensure proper electrolysis was observed.

Chapter 3

Results and Discussion

Through a combination of controlled experiments, the effects of varying cell configuration and the use of different electrocatalyst materials have been determined. These effects have been correlated to specific values of overpotential parameters which govern the kinetic Tafel Equation derived in Chapter 1. This chapter will develop the analysis of these effects, first by defining the overpotentials, applying the Tafel Equation to aid in the identification of the parameters, and ultimately quantifying the relationship between the overpotential parameters and the experimental conditions imposed in these tests. In doing so, the electrocatalytic properties of RuO_2 nanorods can be determined from the experimental results.

3.1 Overpotential Identification

As previously stated, overpotential is the additional voltage required for water electrolysis to occur beyond the thermodynamic minimum cell voltage ($V_{min} = 1.23V$). These overpotentials occur for a variety of reasons including the use of inactive electrocatalyst materials, increased resistances between system components, and the limitations imposed by the mass transfer of species. The lower the overpotential required in a PEM water electrolysis sys-

tem, the greater the cell efficiency. The overpotentials measured in this investigation will be used to compare the different electrocatalysts and their configurations. This study will also attempt to associate a change in the overpotential with a change in system configuration. A J-V polarization curve will be used to determine the overpotential values. These values are determined by developing a "line of best fit" equation, in the form of Equation 1.42, for the experimental polarization curves. A single change in the cell configuration can then be quantified by the change in value of the corresponding overpotential. A description of each overpotential parameter and the methods used in this analysis will be presented in the following sections.

3.2 Kinetic Equation of PEM Water Electrolysis

The Tafel Equation, derived in Chapter 1, represents an exponential relationship between a cell's overpotential and current density. The final equation derived in Chapter 1, Equation 1.42 and given again here, will be used as a working formula for the description of water electrolysis in a PEM cell:

$$J = \frac{J_o \left(exp \left[\frac{(Vop - 1.23)\alpha F}{RT} \right] \right)}{1 + \left(\frac{J_o}{J_l} exp \left[\frac{(Vop - 1.23)\alpha F}{RT} \right] \right)} \tag{3.1}$$

The three parameters found in the above equation represent separate aspects of the (overpotential - current density) relationship. The exchange current density J_o, previously defined in Section 1.3.5, is an indication of the number of surface states available for the electrochemical reactions to occur. A large value for the exchange current density will lead to a greater maximum current density if other overpotentials do not hinder the electrolysis

reaction from occurring.

The limiting current density, J_l, is the maximum current density the specific electrochemical system can achieve as a result of the mass transfer of reactant and product species. When the oxidation or reduction of a species is occurring at a rate equal to the arrival rate of a species being transported to the electrocatalysts surface, this step is rate determining [14]. The three modes of mass transport described in Section 1.3.7 are migration, diffusion, and convection. When discussing these phenomena as rate limiting, each of these modes will be considered and their contributions weighed.

The charge transfer coefficient α, previously defined in Section 1.3.4, represents the partial electrostatic potential which effects the rate of the reaction [14]. As a measure of the symmetry of the quantum energy barrier, this factor represents which reaction direction is favored, forward or backward. This behavior is influenced by enhanced movement across the energy barrier by a charged species. A change in α changes the slope of the exponential curve, and as α approaches 1 the rate increases significantly. These three parameters are used to quantify the overpotential measured so the various electrolyzer cell configurations can be compared.

3.3 Analysis Method

The parameters identified above were determined by an analysis method of minimizing the sum of the squared error. The experimentally obtained polarization curves were plotted with a Microsoft Excel Spreadsheet. Using Equation 3.1, similar curves were produced by assigning values for the overpotential parameters. The sum of the squared error was calculated for the fitted curve to the physical curve using the following equation.

$$SSE = \sum_{i=Vopmin}^{Vopmax} (J_p(i) - J_f(i))^2 \tag{3.2}$$

J_p is the measured current density for the applied voltage range of 0V to 2.5V and J_f is the current density calculated using Equation 3.1 for the same applied voltage range.

This sum of the squared error is then minimized using the Excel Solver GRG nonlinear method. This solver method varies the three overpotential parameters in order to minimize the sum of the squared error. Since this method, at it's best, locates locally optimal solutions, the overpotential coefficients were first varied manually to set the initial conditions close to the minimized values. Depending on the configurations being compared, specific constraints were applied. For example, the effect of varying electrocatalyst materials does not vary the mass transport of species and therefore the limiting current density, J_l, is held constant for this particular analysis. Due to the large variability of values of these overpotential parameters in the literature, many authors use these parameters to fit models derived from theory to their experimental data [3]. Fitting practices of this nature were utilized in much of the literature considered for this study. See references (11,29,53,54).

The resulting analytically derived overpotential parameters of each set of experiential data are used in the following sections to aid in the discussion and comparison of the physical operation of each electrolyzer cell configuration. The changes applied to the experiential trials include separating the GDL from the electrocatalyst surface, separating the electrocatalyst surface from the Nafion membrane, and varying the electrocatalyst material of these dissembled membrane electrode configurations. The overpotential parameter, limiting current density (J_l), accounts for the separation of layers. Exchange current density (J_o) represent a change in the number of surface sites available for the electrolysis reaction [53, 54]. The charge transfer coefficient (α) represents the enhancement of electric field

effect which increase reaction rate [14]. A table containing the values of these parameters for the configurations of interest will be included in each section and discussed further. Diagrams of the various configurations discussed will also be presented in each section. A sketch of the various MEA configurations implemented over the course of this study can be found in Figure 3.1 below.

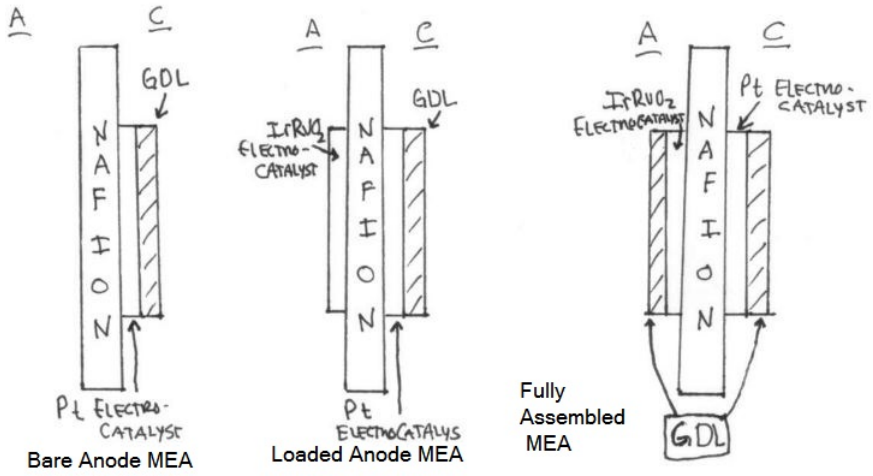

Figure 3.1: Identification of Various MEA Configurations

3.4 Separation of Gas Diffusion Layer From Electrocatalyst Surface

The experimental results presented and discussed in this section are of various electrolyzer cell configurations in which the direct use of $IrRuO_2$ as an anode electrocatalyst on the Nafion membrane is kept constant. This experiment includes the use of both the fully assembled MEA and loaded anode MEA configurations shown in Figure 3.1. Therefore the GDL is either attached directly to the electrocatalyst surface of the MEA or positioned as a

separate layer. Figure 3.2 is a sketch of the general layer stack order implemented in these experiments. The water electrolysis J-V plot is shown in Figure 3.3.

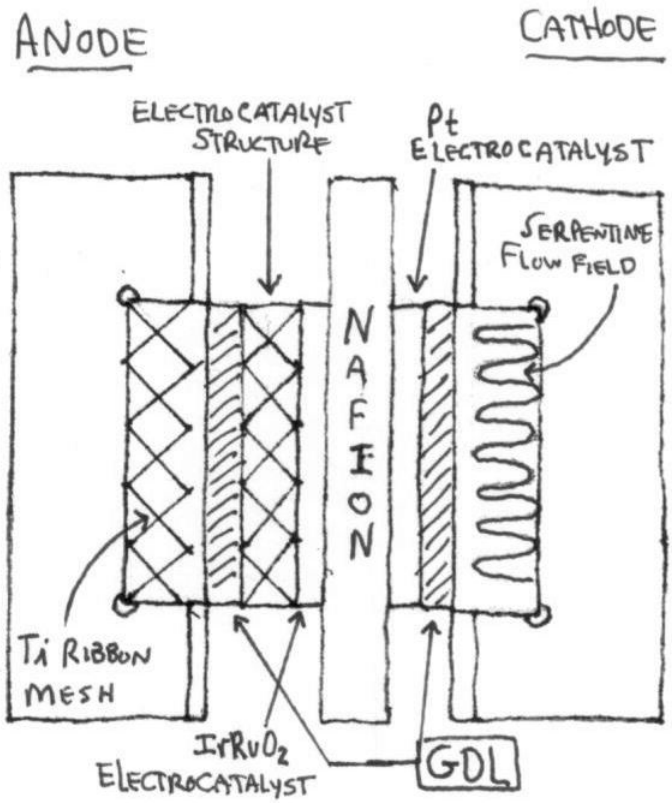

Figure 3.2: Diagram of general layer stack order implemented in these experiments.

As Figure 3.3 shows, the fully assembled MEA has the greatest overall performance. The overall effect of the separation of the GDL from the MEA is evident when comparing the curve represented by the squares and the curve represented by the diamonds. The configuration with the separated GDL experiences overpotential likely caused by increased resistance between the electrocatalyst surface and the GDL. This is evident as an increase in applied voltage is required of this configuration relative to the fully assembled MEA configuration. The overall result of the effect of this separation is not represented by the electrochemical kinetics alone and therefore the overpotential parameter values do not provide a sufficient explanation of the physical phenomena. The effect of the separation is a significant increase in the resistance between the anode bipolar plate and electrocatalyst surface, and hinders the movement of electrons. The effect of this separation is important to consider because the disassembly of the commercial 5-layer MEA is required to test the electrocatalyst materials of interest.

The inclusion of the electrocatalyst layers of interest in this investigation was accomplished by placing a Ti ribbon mesh anode catalyst structure in between the GDL and the anode electrocatalyst surface as illustrated in Figure 3.2. The configuration including a catalyst structure covered with a mixed metal oxide (MMO) of Ir/Ta corresponds to the triangle plotted curve in Figure 3.3. The same configuration including the Ti ribbon mesh catalyst structure stripped of it's MMO, corresponds to the X plotted curve. These curves are within measurable error of each other which leads to the conclusion that the electrocatalyst materials are not significant when in the presence of the $IrRuO_2$ electrocatalyst, which is directly loaded onto the Nafion membrane. It is expected that the Ir/Ta covered catalyst structure will out perform the same structure covered by Ti. This expectation is supported by the results discussed in Section 3.7. A comparison of these results to the response of the separation of the GDL from the electrocatalyst surface shows that the installation of

the ribbon mesh anode catalyst structures does lower the significant resistance previously experienced. This is accomplished by providing a path of lower resistance between the GDL and electrocatalyst surface. Therefore the effect of separating the GDL from the electrocatalyst surface of an MEA is expected to lower overall performance, though the ribbon mesh anode catalyst structure provides enough conductivity for the reactions to not be hindered too heavily.

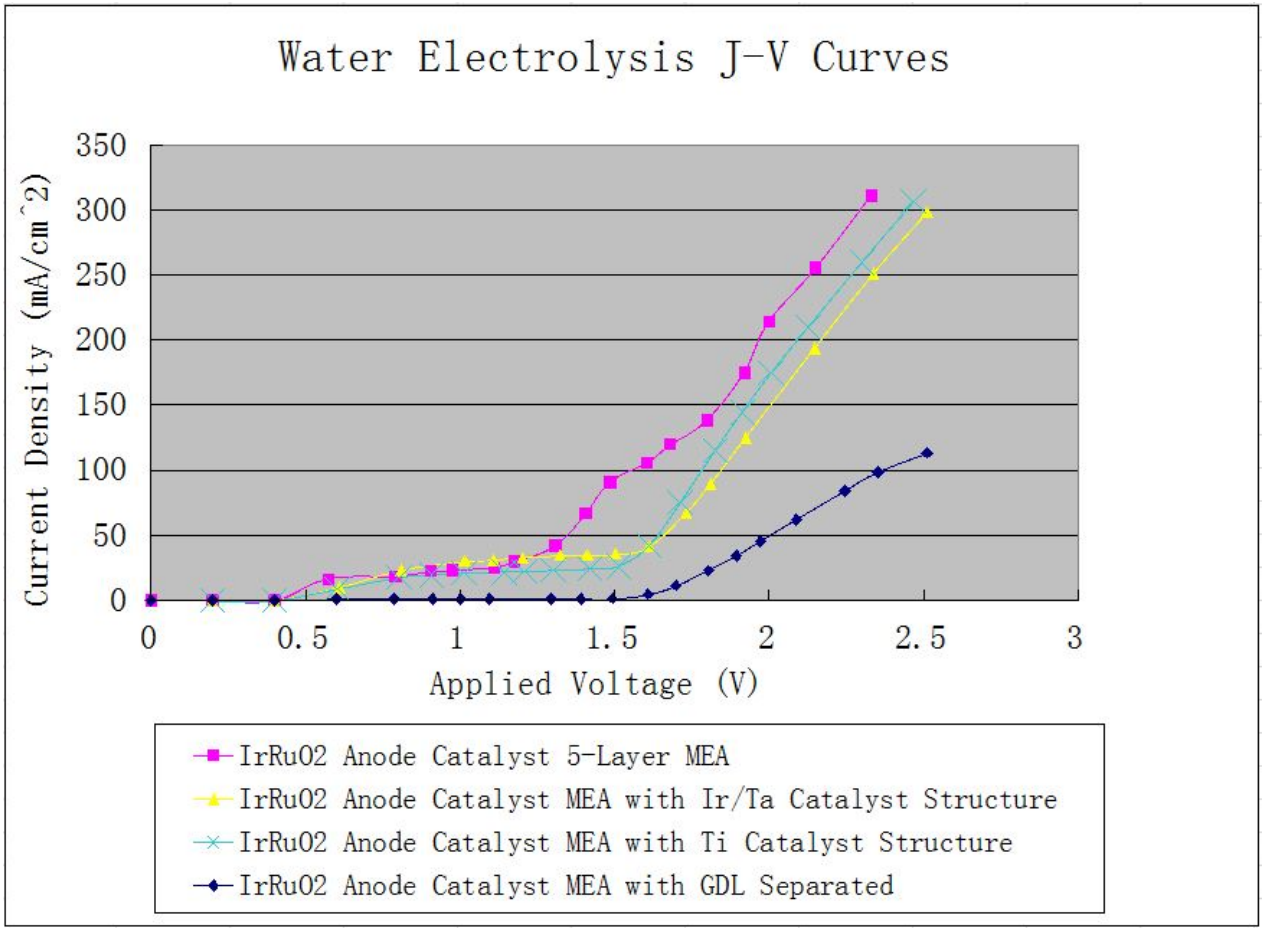

Figure 3.3: Water electrolysis J-V plot of applied voltage vs. current density for various electrolyzer cell configuration.

3.5 Separation of Electrocatalyst Surface From Nafion Membrane

The experimental results presented and discussed in this section result from comparing the effect of separating the electrocatalyst material from the Nafion membrane of the MEA. The J-V plot in Figure 3.4 contains two curves analyzed in the previous section, as well as the additional curve represented by + marks, which is the resulting behavior of the $IrRuO_2$ electrocatalyst material separated from the Nafion membrane as well as the GDL. The configuration the Nafion layer used is illustrated in Figure 3.1 as the bare anode MEA. Results from the previous section showed an additional electrocatalyst material layer placed next to the $IrRuO_2$ loaded anode electrocatalyst did not appear to provide any additional electrocatalytic activity. The ability to exchange various non-attached electrocatalyst material layers is required to investigate the electrocatalytic ability of unattached RuO_2 Nanorods.

The effect of a separation between the electrocatalyst surface and GDL can be seen by comparing the diamond plotted and + plotted polarization curves in Figure 3.4. The + plot corresponds to the configuration where the 5-layer MEA is fully disassembled on the anode side, resulting in a separation between the GDL, electrocatalyst layer and Nafion membrane. The same $IrRuO_2$ electrocatalyst material is used in both cases.

The plot shows a decrease in performance as a result of the additional separation of the electrocatalyst surface and Nafion membrane. Table 3.1 includes the values of the overpotential parameters corresponding to this cell's configuration. The limiting current density parameter, J_l, which has been described in Chapter 1 to be dependent on the diffusion of species, is effected by the separation of the electrocatalyst material and the Nafion membrane. This separation causes a decrease in limiting current density, J_l. This

effect can be interpreted as a result of increased diffusion length between the reaction sites of the electrocatalyst surface and the Nafion membrane. Therefore, the diffusion of hydronium ions produced at the electrocatalyst surface becomes a limiting factor of the water electrolysis reaction for this cell configuration.

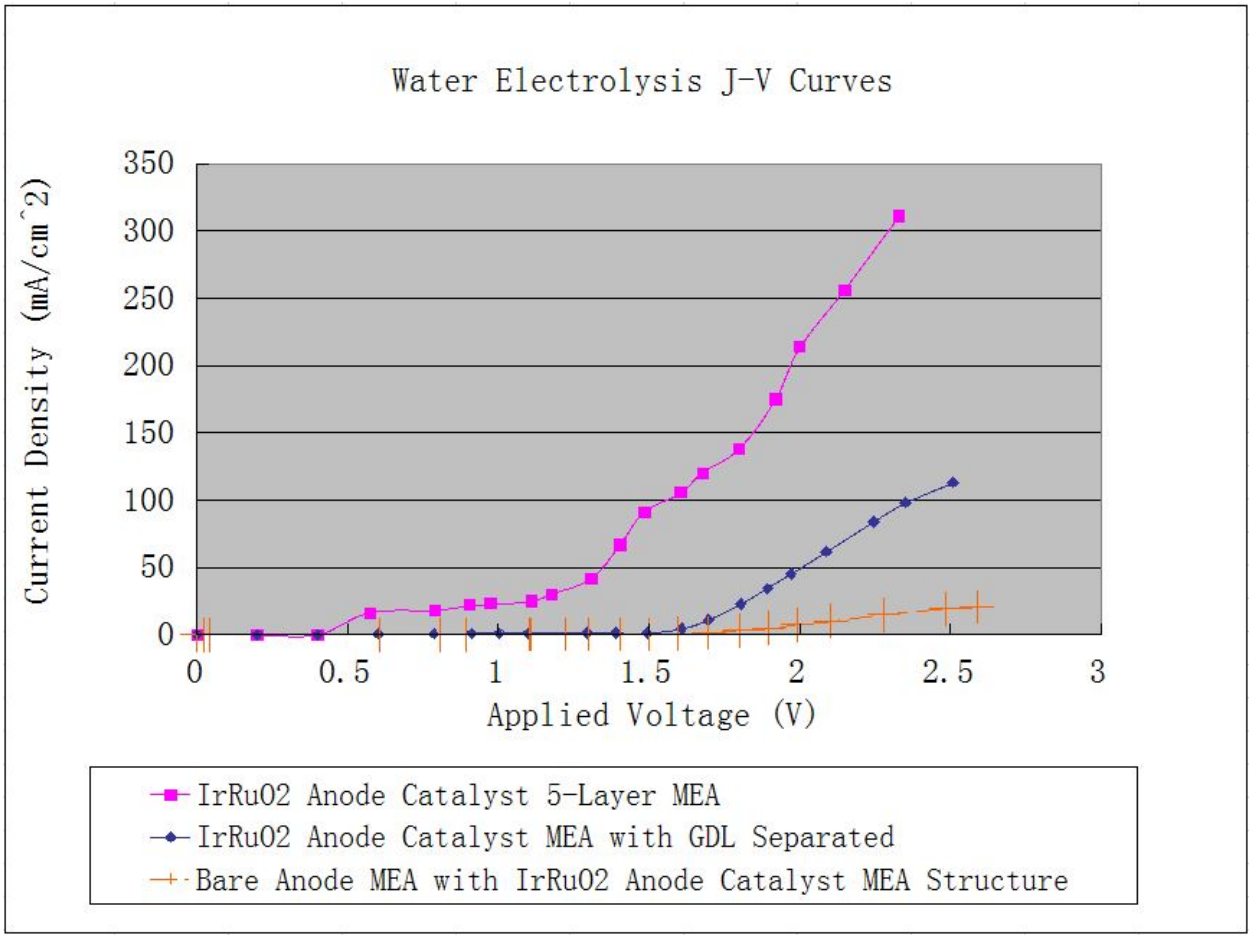

Figure 3.4: Water electrolysis J-V plot of applied voltage vs. current density for various electrolyzer cell configuration.

Overpotential Parameter→ Cell Configuration↓	Exchange Current Density J_o	Charge Transfer Coefficient α	Limiting Current Density J_l
Loaded Anode MEA	1.0000	0.1008	269.7436
Bare Anode MEA with $IrRuO_2$ Loaded MEA Catalyst Structure	1.0000	0.1008	18.4865

Table 3.1: Table of Overpotential Parameter Values

The importance of a close contact between the electrocatalyst surface and the Nafion membrane has been stressed by Wilson and Gottesfeld. They used impedance analysis to show that direct application of the electrocatalyst material on the Nafion membranes improves the interfacial continuity between the membrane and electrocatalyst [55]. Catalyzed membranes have been shown to facilitate ion transport and reduce internal resistance of the MEA which increases the overall activity of the reaction. It is essential to ensure optimal connection between the membrane and electrocatalyst to encourage good ion transport. This is because the conductivity of ion through the Nafion membrane is several orders of magnitude less than the conductivity of electrons in the carbon cloth GDL. Ionic transport limits the reaction, and overall system performance, much more than electron transport does [56].

3.6 Implementation of a Catalyst Guard

A catalyst guard was inserted into the cell configuration in order to further study the effects of layer separation. The catalyst guard insures the spatial separation of electrolyzer cell layers. Appendix E contains the drawing of this catalyst guard which is 1mm thick and is made of a non-electrically conducting plastic. This section analyzes the results of this modification.

3.6.1 Use of a Catalyst Guard to Separate the Electrocatalyst Material Layer and Nafion Membrane

The catalyst guard was initially inserted into the cell configuration in order to develop a better understanding of the effect of separating the electrocatalyst material layer from the Nafion membrane. Figure 3.5 is a sketch of this cell configuration.

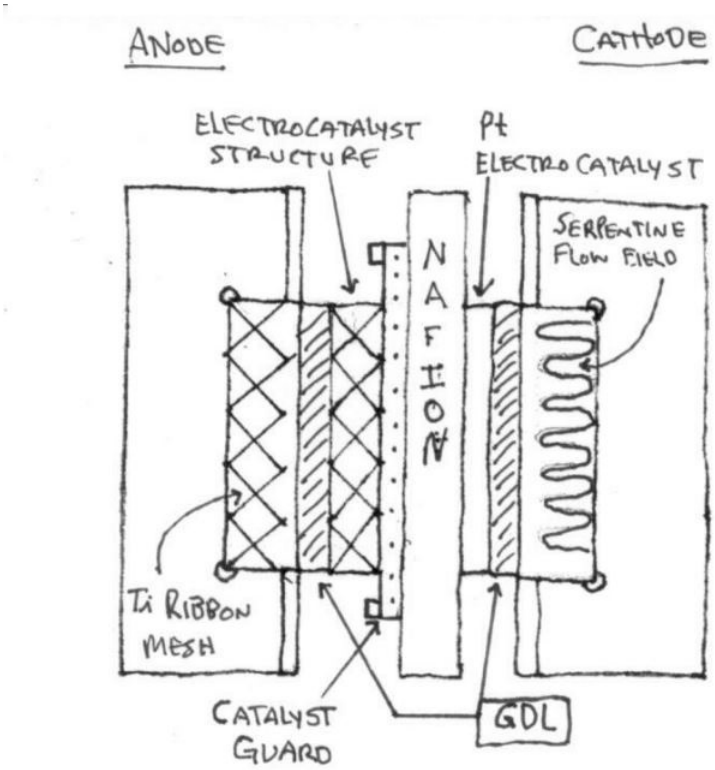

Figure 3.5: Diagram of general layer stack order including the Catalyst Guard implemented in these experiments.

Figure 3.6 contains the water electrolysis J-V plot which compares the polarization curve of this configuration, represented by the squares, to the polarization curve of the same cell configuration without the inclusion of the catalyst guard, represented by the triangles. As the plot shows, placement of the catalyst guard between the electrocatalyst material layer and the Nafion membrane resulted in a complete shut down of the water electrolysis reaction. The limitation of ionic transfer between the electrocatalyst surface and Nafion membrane caused by the catalyst guard explains these results. The separation of the electrocatalyst material layer from the Nafion membrane has a great effect on the half reactions, to the point that no reaction occurs. Therefore the limiting current density overpotential parameter, which represents this mass transfer, will be addressed when analyzing the RuO_2 nanorods as a separated electrocatalyst material layer.

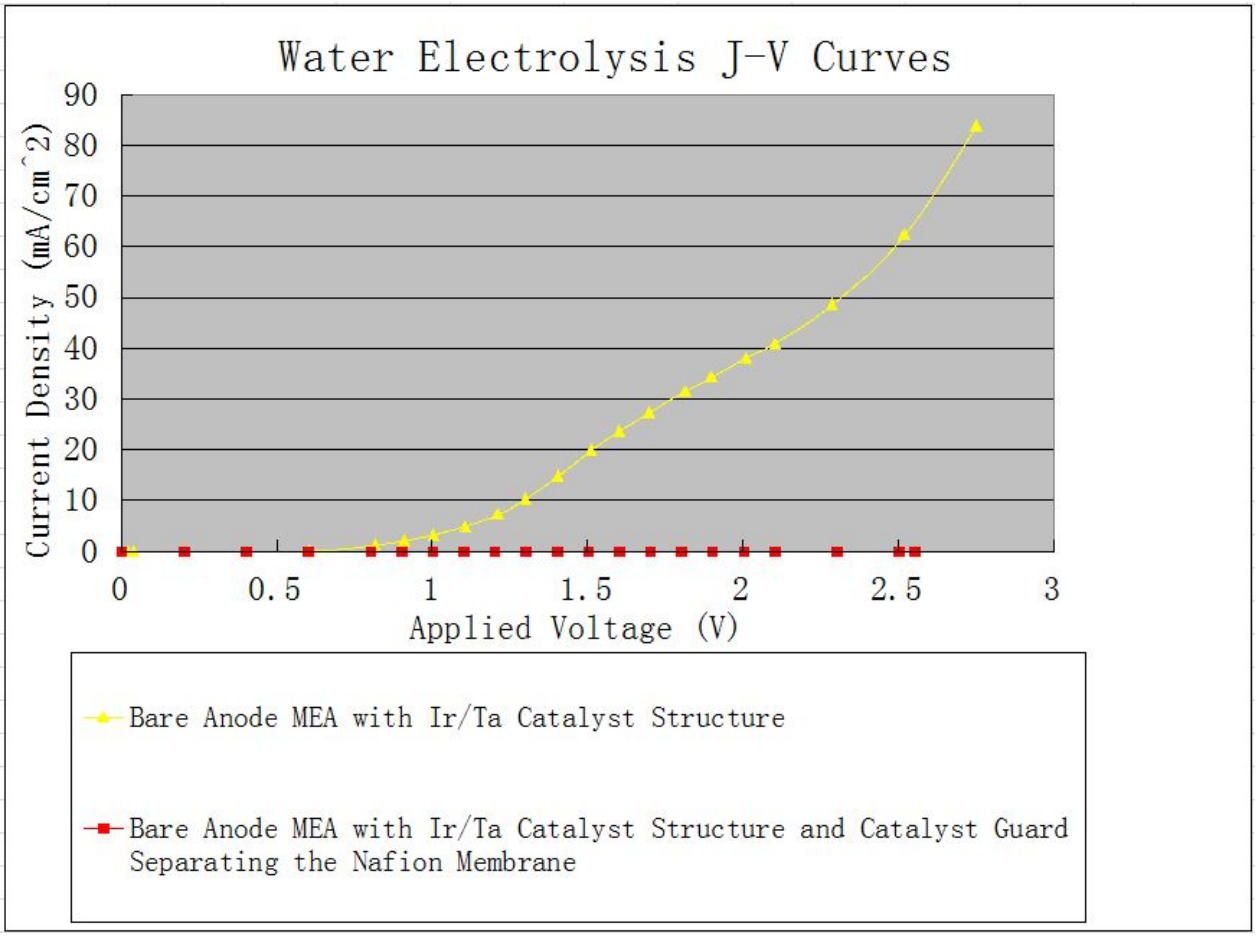

Figure 3.6: Water electrolysis J-V plot of applied voltage vs. current density for various electrolyzer cell configuration.

3.6.2 Use of a Catalyst Guard to Separate the GDL and Electrocatalyst Material Layer

The catalyst guard was then inserted into the cell configuration in order to develop a better understanding of the effect of separating the GDL from the electrocatalyst material layer. This study examined the effect of placing the catalyst guard between the GDL layer and the Ir/Ta ribbon mesh anode catalyst structure. In both configurations studied, the Ir/Ta

catalyst structure made contact to the $IrRuO_2$ anode catalyst material attached to the Nafion membrane. The only modification made to the cell configuration in this study was the placement of the catalyst guard between the GDL and ribbon mesh anode catalyst structure. Figure 3.7 contains the water electrolysis J-V plot which compares the polarization curve of these two configurations. The configuration which included the placement of the catalyst guard is represented by the triangles, where as the polarization curve of the cell configuration without the catalyst guard is represented by the diamonds. As the plot shows, placement of the catalyst guard between the GDL and electrocatalyst material layer exhibits significant reduction of the overall cell performance. This effect of increasing the separation between the GDL and electrocatalyst structure does not completely limit the water electrolysis reaction, though there is a significant effect. The factors contributing to this effect are more complex than a single electrochemical kinetic equation can model and therefore these results ultimately prove that an unobstructed interface between the electrocatalyst and GDL does maximize cell performance.

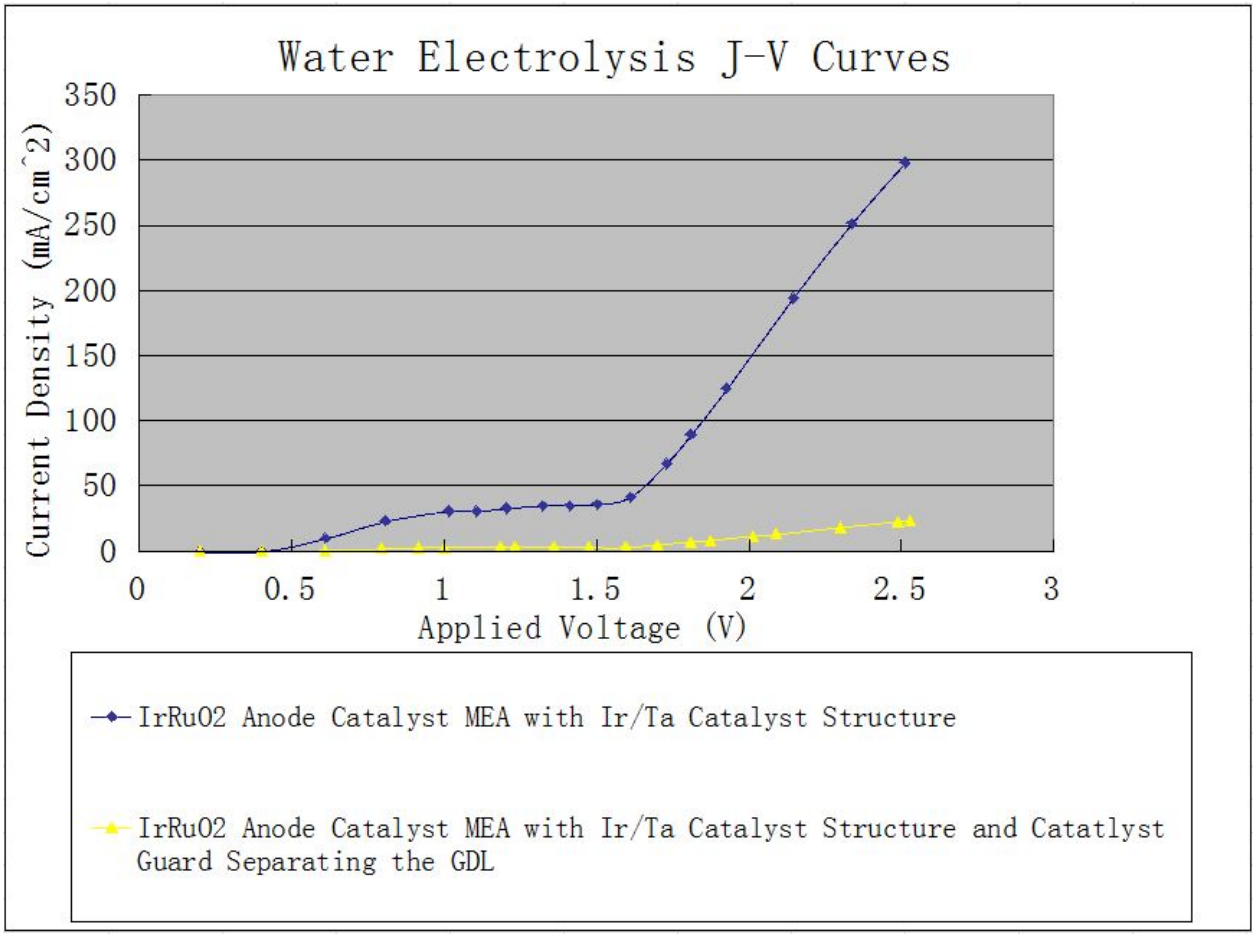

Figure 3.7: Water electrolysis J-V plot of applied voltage vs. current density for various electrolyzer cell configuration.

3.6.3 Comparing Electrocatalytic Materials while Separating the GDL and Electrocatalyst Material Layer with a Catalyst Guard

The electrocatalytic behavior exhibited in the previous section by the Ir/Ta ribbon mesh anode catalyst, separated from the GDL by a catalyst guard, encouraged the comparison of electrocatalytic materials while implementing this cell configuration. It is believed that the

increased separation of the GDL and electrocatalyst material layer, provided by the catalyst guard, promotes the electrocatalytic behavior of the material covering the ribbon mesh anode catalyst structure to be exhibited. Therefore, the performance of the electrocatalyst materials, RuO_2 nanorods and Ir/Ta, were compared while implemented in the catalyst guard separated cell configuration. In both configurations studied, the catalyst guard separated the GDL and ribbon mesh anode catalyst structure. The only modification made to the cell configuration in this study was the variation of the electrocatalyst material. Figure 3.8 contains the water electrolysis J-V plot which compares the polarization curve of these two electrocatalyst materials. The performance of the RuO_2 nanorod decorated Ir/Ta electrocatalyst material is represented by the circles, where as the polarization curve of the of the Ir/Ta electrocatalyst material is represented by the triangles. As the plot shows, the RuO_2 nanorod decorated Ir/Ta electrocatalyst out performed the Ir/Ta electrocatalyst.

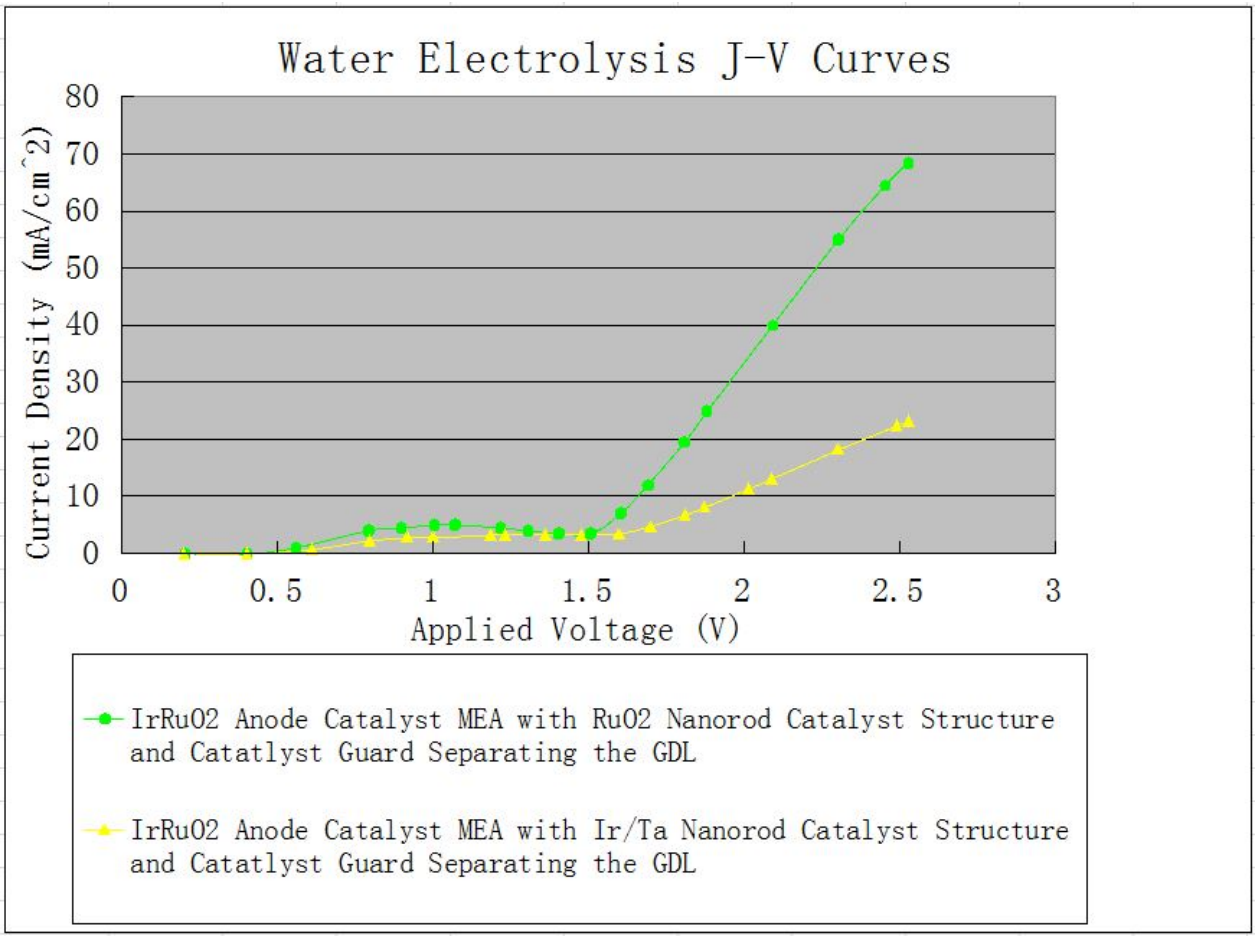

Figure 3.8: Water electrolysis J-V plot of applied voltage vs. current density for various electrolyzer cell configuration.

Table 3.2 contains the overpotential parameter values of the electrocatalyst materials of interest. The exchange current density, J_o, and limiting current density, J_l, are set equal for each of the electrocatalyst materials. This is because these two overpotential parameters should not depend on a change in electrocatalyst material. The consistent use of the ribbon mesh anode catalyst structure and lack of variation in layer separation this experiment contains, reflect these constant experimental conditions. The charge transfer coefficient does vary dependent on the electrocatalyst material. The use of the RuO_2 Nanorod decorated

catalyst structure resulted in an increase in the charge transfer coefficient, α. Therefore, the RuO_2 nanorods provided a greater change in the symmetry of the quantum energy barrier resulting in an increase of charge transport. This change in symmetry is caused by the enhanced electric field produced by the RuO_2 nanorods. This study exposes the enhanced electrocatalytic properties of the RuO_2 nanorods, which will be investigated further in the following sections.

Overpotential Parameter→ Cell Configuration↓	Exchange Current Density J_o	Charge Transfer Coefficient α	Limiting Current Density J_l
Loaded Anode MEA with Ir/Ta Catalyst Structure and C.G.	1.0000	0.0661	268.7647
Loaded Anode MEA with RuO_2 Nanorod Catalyst Structure and C.G.	1.0000	0.0936	268.7647

Table 3.2: Table of Overpotential Parameter Values

3.7 Various Electrocatalyst Materials

The experimental results presented and discussed in this section are of various electrocatalytic materials implemented into a cell configuration in which a ribbon mesh anode catalyst structure is placed directly between the GDL and Nafion membrane. This configuration is illustrated in Figure 3.1 as the bare anode MEA. Figure 3.9 is a sketch of the cell configuration implemented in this experiment. The water electrolysis J-V plot is shown in Figure 3.10 followed by Table 3.3, which contains the various overpotential parameter values for each polarization curve.

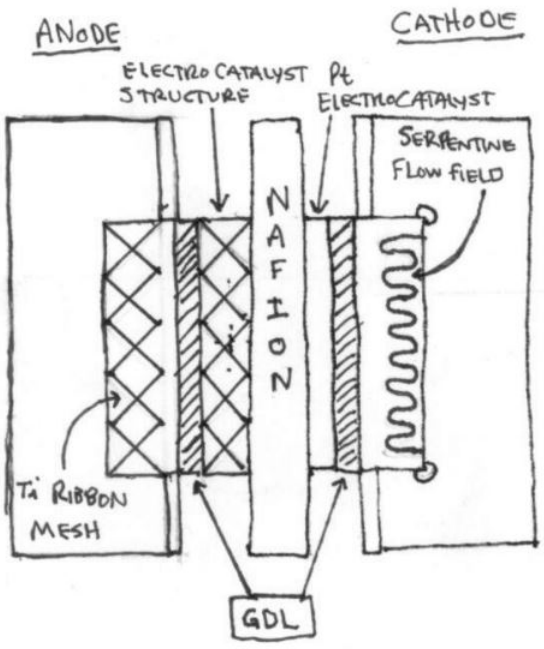

Figure 3.9: Diagram of general layer stack order implemented in these experiments.

This section focuses on the comparison of the electrocatalytic properties of the various materials covering a ribbon mesh anode catalyst structure. The a change in electrocatalytic material is the only variation between the three cases represented in Table 3.3. Electrocatalytic properties are represented by both the exchange current density, J_o, and the charge transfer coefficient, α. These parameters have respective effects on the overpotential-current density relationship as shown in the Tafel Equation (Equation 1.34). The exchange current density, J_o, was previously defined as a frequency factor, representing the number of available surface sites of the catalyst structure, while the charge transfer coefficient, α, is a probability factor correlated to a charged species overcoming the quantum energy barrier. The effect an enhanced electric field has on the charge transfer coefficient has been stated previously.

The resulting overpotential parameter values for the various electrocatalyst materials are included in Table 3.3. The limiting current density is held constant as the change in electrocatalyst material does not effect mass transport of species. The exchange current density is also held constant because the change in electrocatalyst material in this investigation does not represent a significant change the number of available reaction sites. The consistency of the size and shape of the ribbon mesh anode catalyst structure, which these electrocatalyst materials are covering, accounts for the exchange current density values being equal. The focus of this analysis is on the charge transfer coefficient. In comparing the use of the Ir/Ta MMO covered ribbon mesh anode catalyst support, the triangle plotted curve in Figure 3.10, to the use of the Ti covered catalyst support, the X plotted curve, it is evident from both the J-V plot and the comparison of the charge transfer coefficient values, that the Ir/Ta has a greater electrocatalytic ability than that of Ti.

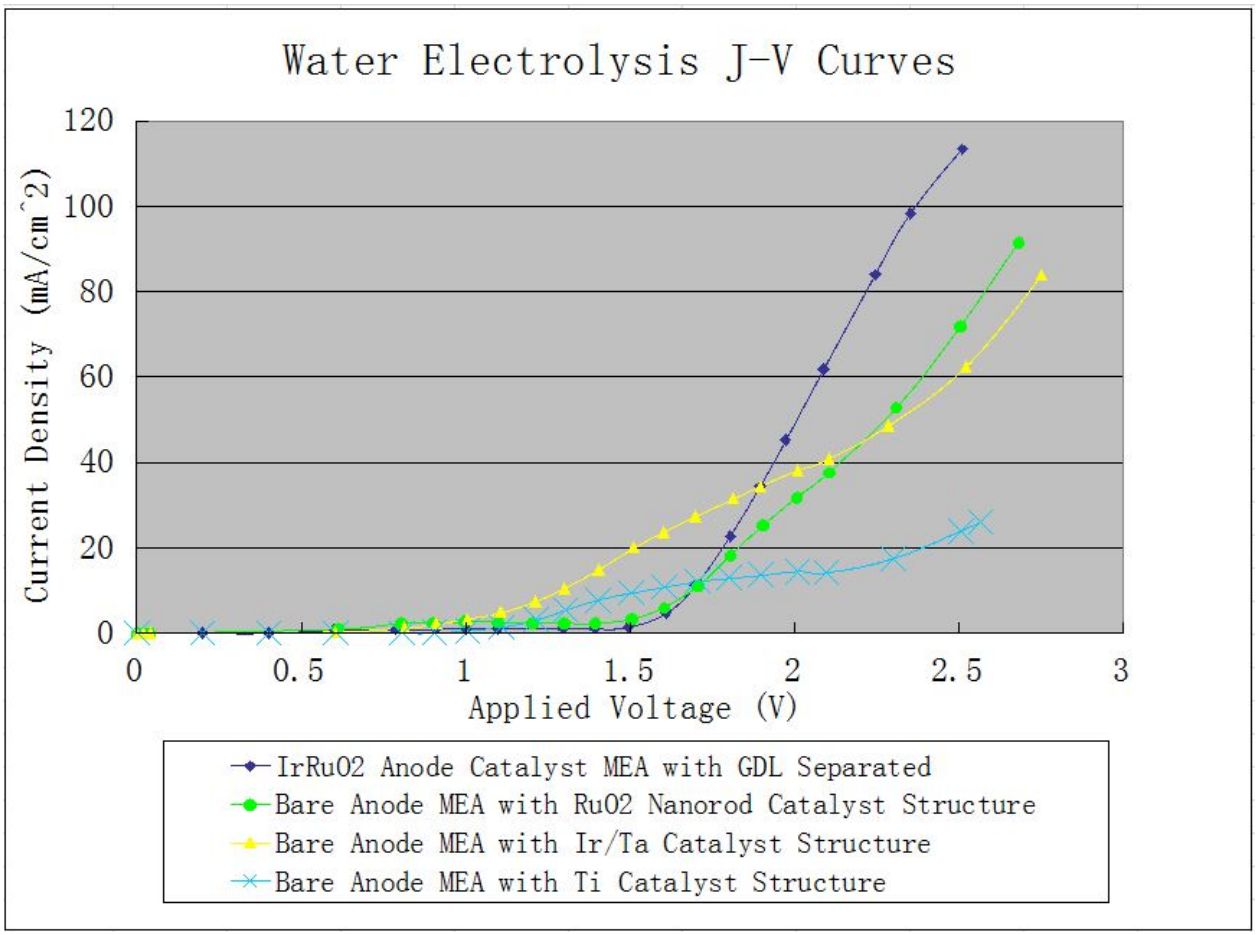

Figure 3.10: Water electrolysis J-V plot of applied voltage vs. current density for various electrolyzer cell configuration.

A comparison between the use of the RuO_2 Nanorod decorated catalyst structure, which corresponds to the circle plotted curve, and the use of the Ir/Ta catalyst structure can then be made. A comparison of the curves plotted in Figure 3.10 is initially inconclusive, as for lower applied voltages, the Ir/Ta electrocatalyst material appears to be more active. At greater applied voltages, around 2.2V, the activity of the RuO_2 Nanorods becomes greater.

A comparison of the overpotential parameter values, included in Table 3.3, provides a greater understanding of the activities observed above. The value of the charge transfer

Overpotential Parameter→ Cell Configuration↓	Exchange Current Density J_o	Charge Transfer Coefficient α	Limiting Current Density J_l
Bare Anode MEA with RuO_2 Nanorod Catalyst Structure	1.7240	0.1067	94.1262
Bare Anode MEA with Ir/Ta Catalyst Structure	1.7240	0.0587	94.1262
Bare Anode MEA with Ti Catalyst Structure	1.7240	0.0335	94.1262

Table 3.3: Table of Overpotential Parameter Values

coefficient, α, corresponding to the use of the RuO_2 nanorod electrocatalyst material is double that of the Ir/Ta electrocatalyst. As previously stated, α represents the probability factor of the electrochemical reactions to occur. In fact, this parameter provides a clear explanation of the plotted behaviors in Figure 3.10. An increased α is representative of an increase in electron movement across the energy barrier aided by an enhanced electric field effect. This effect will become greater has the potential difference between the anode and cathode electrocatalyst material is increased due to an increase in applied voltage. This explains the increase in activity of the RuO_2 nanorods as the applied voltage is increased. The RuO_2 nanorods provide an enhanced electric field effect, which ultimately increases the cell performance at higher applied voltages. It is suggested that the increased current densities achieved by the Ir/Ta and Ti electrocatalyst materials can be identified as leakage current caused by the lack of an oxide interface. The RuO_2 nanorod decorated ribbon mesh anode catalyst structure has an interfacial oxide layer between the RuO_2 nanorods and the ribbon mesh anode structure. Both the Ir/Ta and Ti covered ribbon mesh anode structures lack this leakage current preventing oxide.

3.8 Theoretical Behavior of RuO_2 Nanorods Corrected for Mass Transfer Limitation

The experiential evidence of cell configuration modification, provided by the analysis discussed in previous sections, leads to the ability to compare the behaviors of different cell configurations. Correction factors are formulated to compensate for a modification in cell configuration, such as the separation of the electrocatalyst material layer from the Nafion membrane. This separation results in a variation in values of the limiting current density overpotential parameter. The values of this overpotential parameter can be corrected for in order to compensate for diffusion limitations caused by the separation of layers. Therefore the measured results of the separated RuO_2 Nanorod electrocatalyst can be corrected for in order to account for the mass transfer limitation caused by this separation. The resulting corrected behavior can be compared with other measured results which correspond to similar cell configurations.

A correction factor of J_l, is calculated from the comparison of the $IrRuO_2$ electrocatalyst separated from the Nafion membrane to that of the $IrRuO_2$ electrocatalyst attached to the Nafion membrane, made in Section 3.5. Correcting the separated RuO_2 nanorod electrocatalyst data, using this correction factor, results in a Tafel Equation representing the expected behavior of a MEA containing a RuO_2 nanorod anode electrocatalyst attached to the Nafion membrane.

Figure 3.11 shows the resulting theoretical polarization curve of this configuration, represented by the dash marks. The plot shows a similar relationship between the $IrRuO_2$ loaded anode MEA configuration and the corrected RuO_2 nanorod electrocatalyst behavior as described in the previous section. The increased activity of the RuO_2 nanorod elec-

trocatalyst is again more apparent at increased applied voltages. These results show that RuO_2 nanorods out perform the commercial $IrRuO_2$ as an anode electrocatalyst at applied voltages above 2.2V.

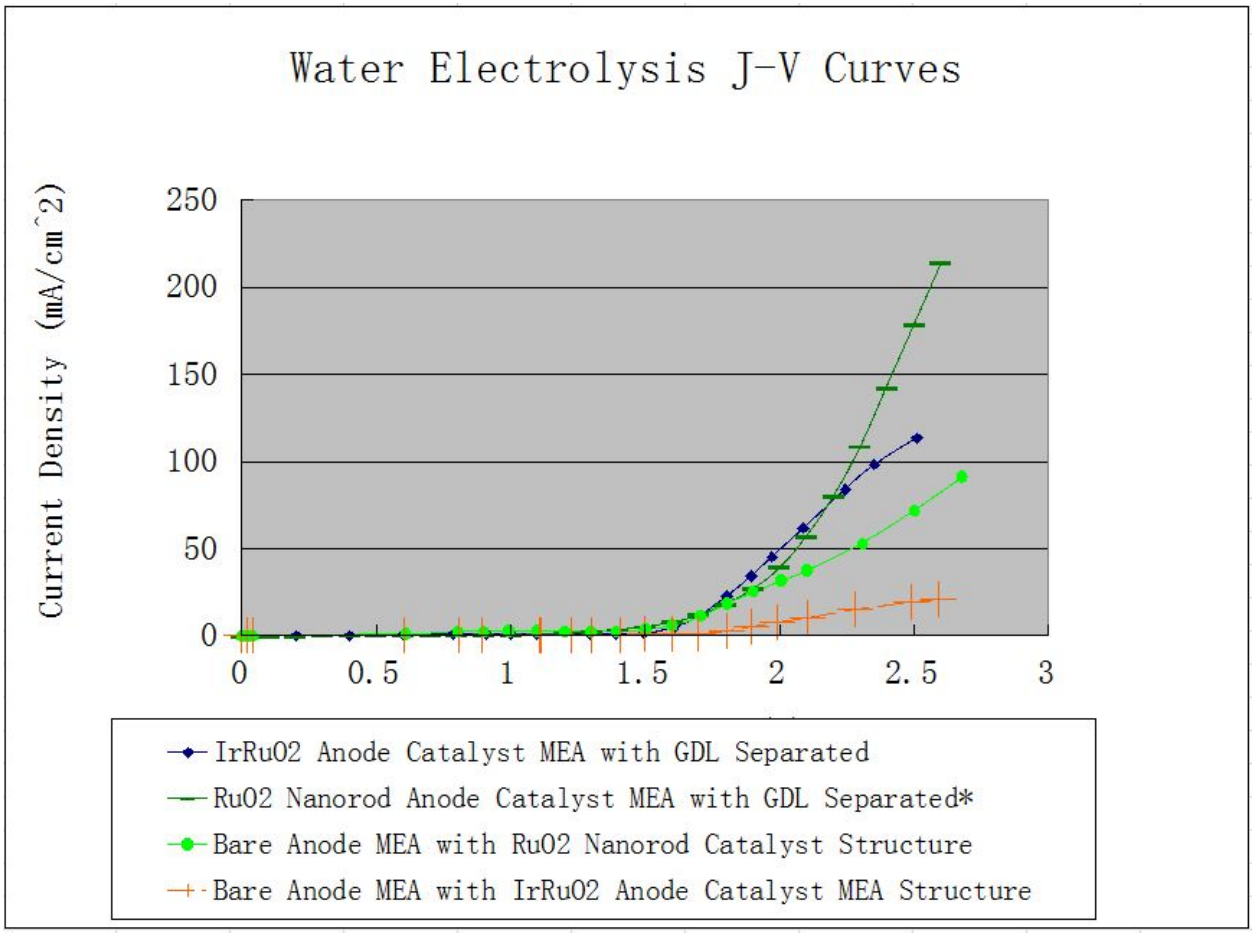

Figure 3.11: Water electrolysis J-V plot of applied voltage vs. current density for various electrolyzer cell configuration.
**Corrected for Mass Transfer Limitations*

Chapter 4

Conclusion

The implementation of RuO_2 nanorods as an anode electrocatalyst in a PEM water electrolyzer cell results in overall enhanced cell performance as the applied voltages increase. The analysis of recorded data representing the physical behavior of the cell, provides a deeper insight into this increased performance. Enhanced electric field effects, attributed to the geometry of the RuO_2 nanorods, are shown to contribute to the enhanced performance. As a result, the RuO_2 nanorods are considered a distinguished electrocatalyst material. The behavior of this electrocatalyst material corrected for the limiting current density overpotential, caused by the separation of the electrocatalyst surface and Nafion membrane, presents the potential of addition enhanced performance that would result from attaching the RuO_2 nanorods directly to the Nafion membrane.

In order to pursue this study further, the theoretical performance of the attached RuO_2 nanorods would need to be compared to the physical behavior of this cell configuration. Though conceivably elementary, the development of processes and procedures required to perform this material loading would require extensive research and development. The main challenge would be to compensate for the high temperatures required for the assembly of the RuO_2 nanorods. Current Nafion membranes begin to melt at temperatures above $100°C$,

where as the assembly of RuO_2 nanorods requires temperatures of at least $460°C$ [41,42,57]. Achieving growth of RuO_2 nanorods on a Nafion membrane would provide the MEA configuration required to perform more comparative experiments.

The use of RuO_2 nanorods as an anode electrocatalyst for PEM water electrolyzer cells will provide material solutions to various obstacles currently limiting the implementation of PEM water electrolysis systems into the current energy infrastructure. Ruthenium could replace Iridium, which is becoming more difficult to obtain, as an electrocatalyst material. The growth method of RuO_2 nanorods could reduce electrocatalyst production costs. The increased surface dimensions, which correspond to geometry of the nanorod structure, would lower the amount of required electrocatalyst material. The enhanced electric field effect of the nanorod tips provide increased reaction rates which have the potential to be intensified through the use of vapor fed PEM electrolyzer cells [49, 51, 58].

The enhanced electrocatalytic properties of RuO_2 nanorods have been proved experimentally. Altogether, the presented work helps to improve the understanding of the use of a nanostructure material as an anode electrocatalyst in a PEM water electrolyzer cell. This facilitates the development of anode electrocatalyst materials.

Appendix A

Scanning Electron Microscope Images of RuO_2 Nanorods

The following SEM images are courtesy of Dr. Micheal Cross, whose is responsible for growing the Nanorods as well as photographing them.

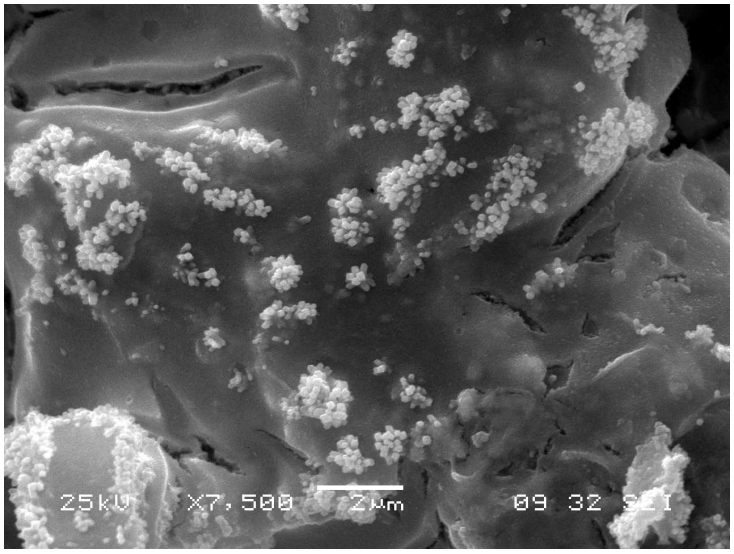

Figure A.1: SEM Image x7,500 Zoom

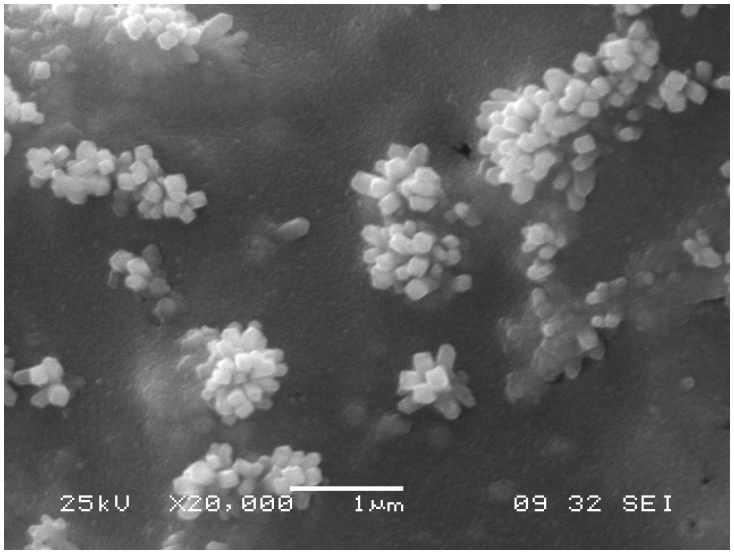

Figure A.2: SEM Image x20,000 Zoom

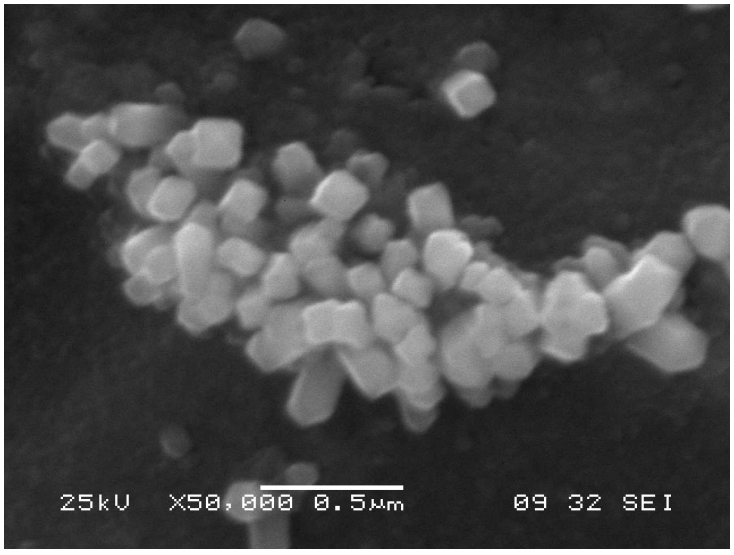

Figure A.3: SEM Image x50,00 Zoom

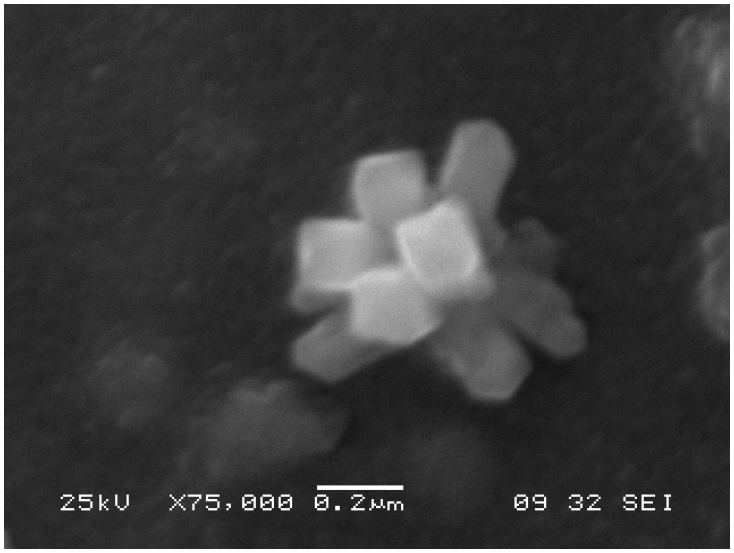

Figure A.4: SEM Image x75,000 Zoom

Appendix B

PEM Water Electrolysis System Diagrams

The closed loop water supply system diagram and circuit diagram are provided in the following sections.

B.1 Closed Loop Water Supply System Diagram

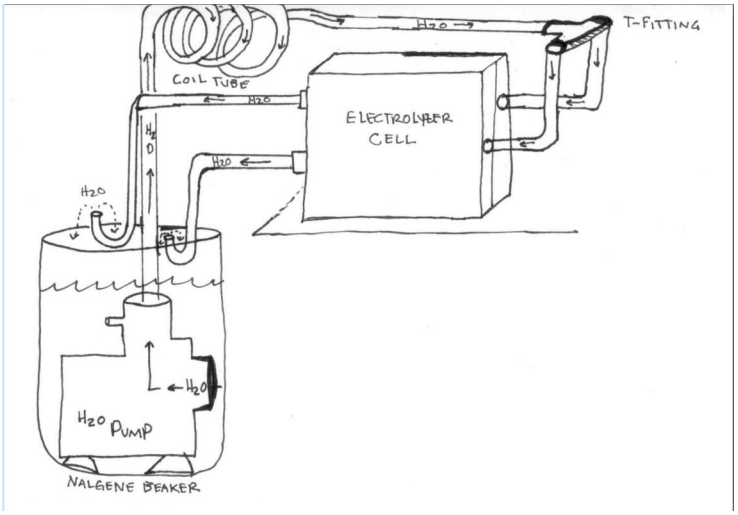

Figure B.1: Diagram of Closed Loop Water Supply System

B.2 Circuit Diagram of PEM Water Electrolysis System

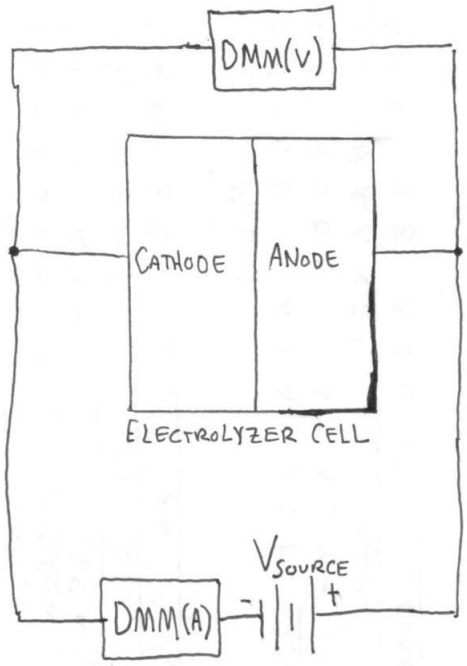

Figure B.2: Circuit Diagram of PEM Water Electrolysis System

Appendix C

Cell Assembly Images

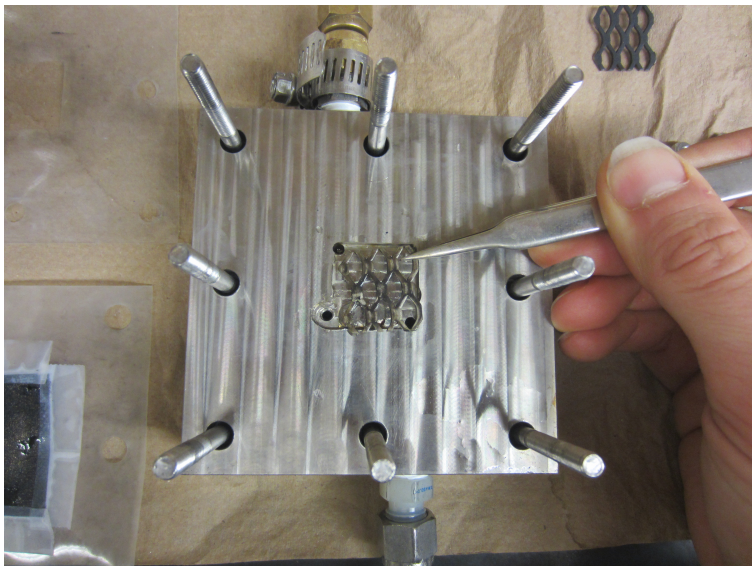

Figure C.1: Anode Bipolar Plate with bolts and Ti ribbon mesh anode flow field fitting

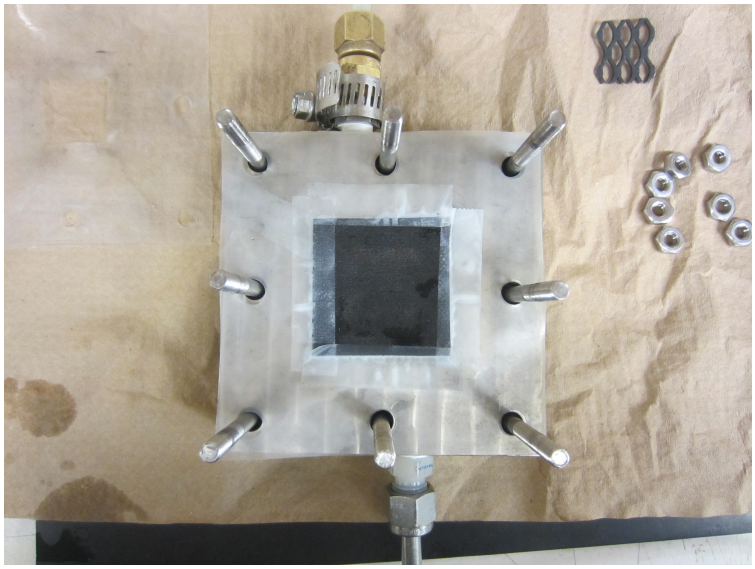

Figure C.2: Anode gasket and GDL

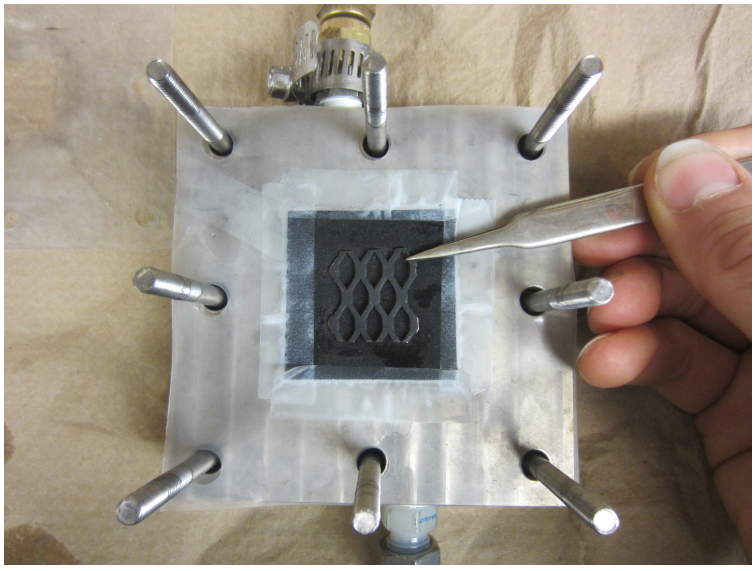

Figure C.3: Anode Electrocatalyst Structure, in this case the Telpro MMO ribbon mesh anode

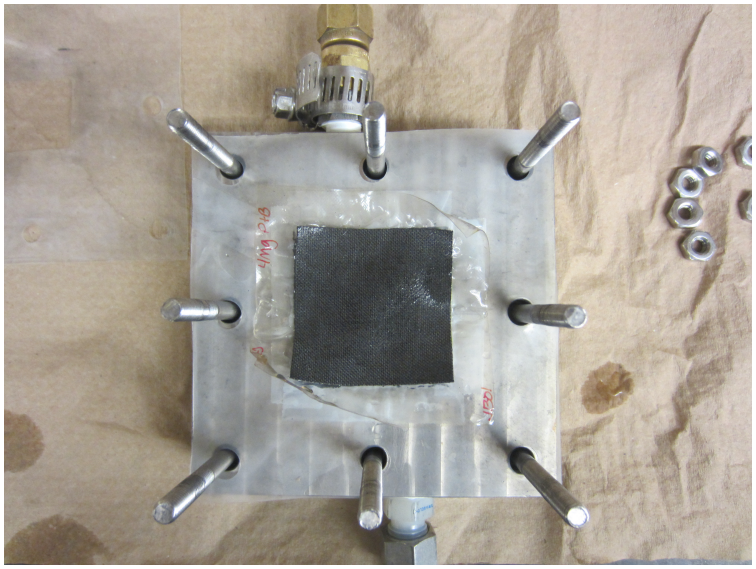

Figure C.4: MEA with cathode GDL facing up, note the curling edges

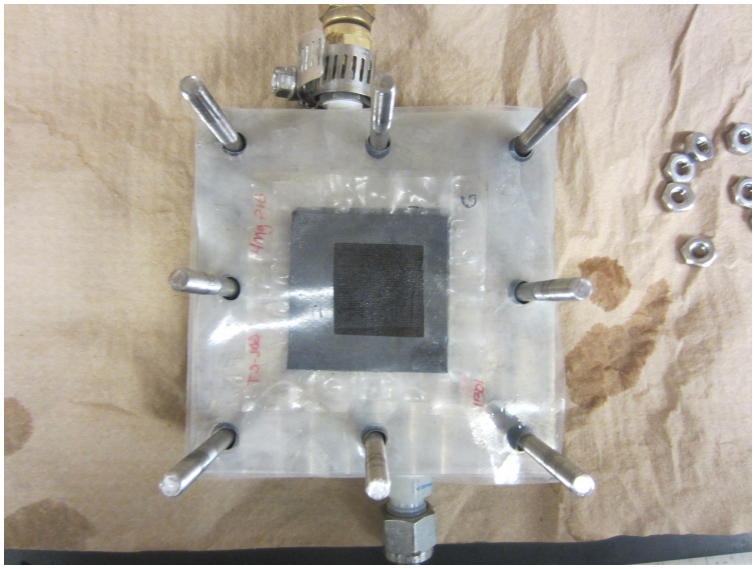

Figure C.5: Cathode Gasket

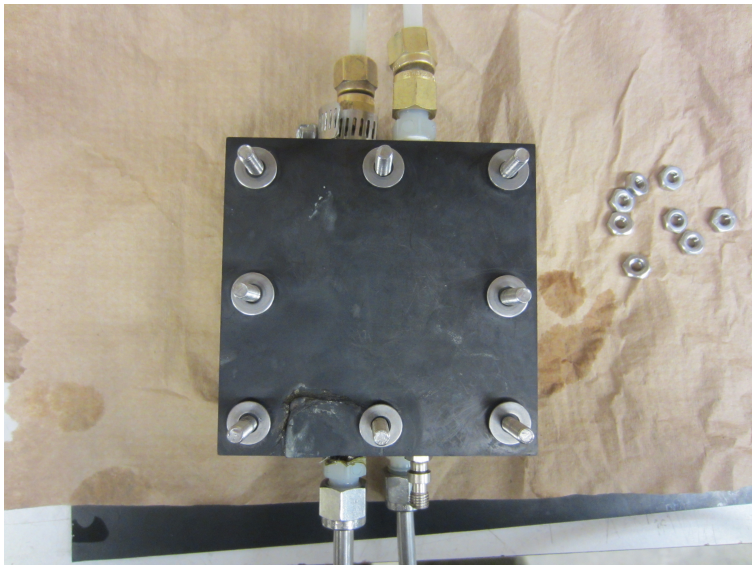

Figure C.6: Cathode Bipolar Plate with bolt fittings and washers

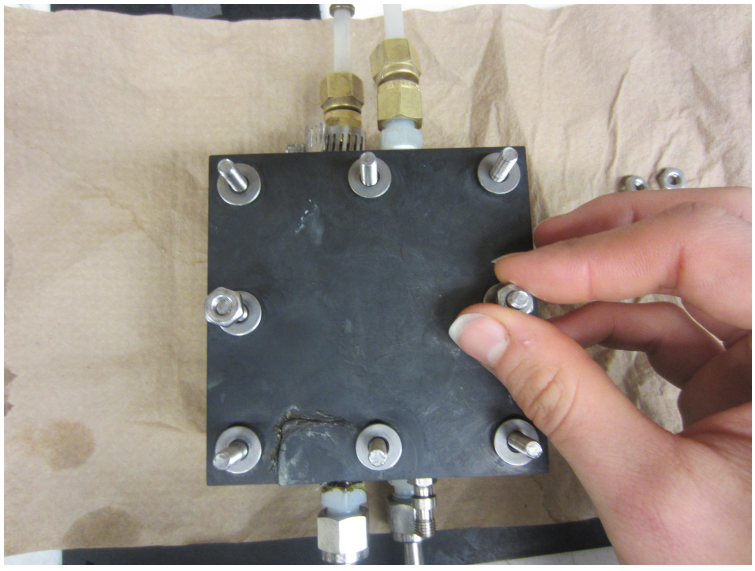

Figure C.7: Finger Tightening Nuts

Appendix D

Sample Data Sheet

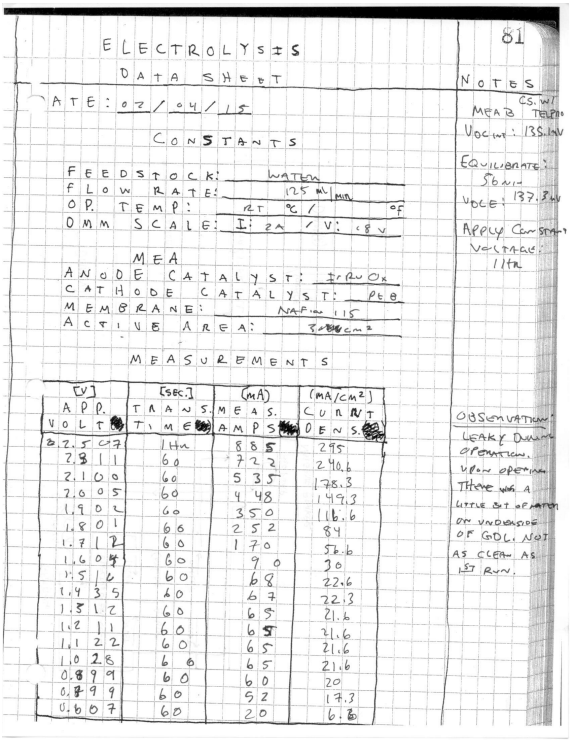

ELECTROLYSIS

DATA SHEET

81

DATE: 07 / 04 / 15

CONSTANTS

FEEDSTOCK: WATER
FLOW RATE: 125 mL/min
OP. TEMP: RT °C / °F
OMM SCALE: I: 2A / V: 1.8 V

MEA
ANODE CATALYST: IrRuOx
CATHODE CATALYST: Pt B
MEMBRANE: NAFion 115
ACTIVE AREA: 5 cm²

MEASUREMENTS

[V] APP. VOLT	[SEC.] TRANS. TIME	(mA) MEAS. AMPS	(mA/cm²) CURR DENS.
2.507	14m	885	295
2.311	60	723	240.6
2.100	60	535	178.3
2.005	60	448	149.3
1.902	60	350	116.6
1.801	66	252	84
1.717	60	170	56.6
1.609	60	90	30
1.516	60	68	22.6
1.435	60	67	22.3
1.351	60	65	21.6
1.211	60	65	21.6
1.122	60	65	21.6
1.028	60	65	21.6
0.899	60	60	20
0.799	60	52	17.3
0.607	60	20	6.6

NOTES

MEAS. CS. W/ TEMP
VOC int: 135.1mV
EQUILIBRATE: 5 min
VOCE: 137.8mV
APPLY CONSTANT VOLTAGE: 1.1V

OBSERVATIONS:
LEAKY DURING OPERATION. UPON OPENING THERE WAS A LITTLE BIT OF WATER ON UNDERSIDE OF GDL. NOT AS CLEAR AS 1ST RUN.

Figure D.1: Sample Data Sheet

Appendix E

Catalyst Guard Drawing

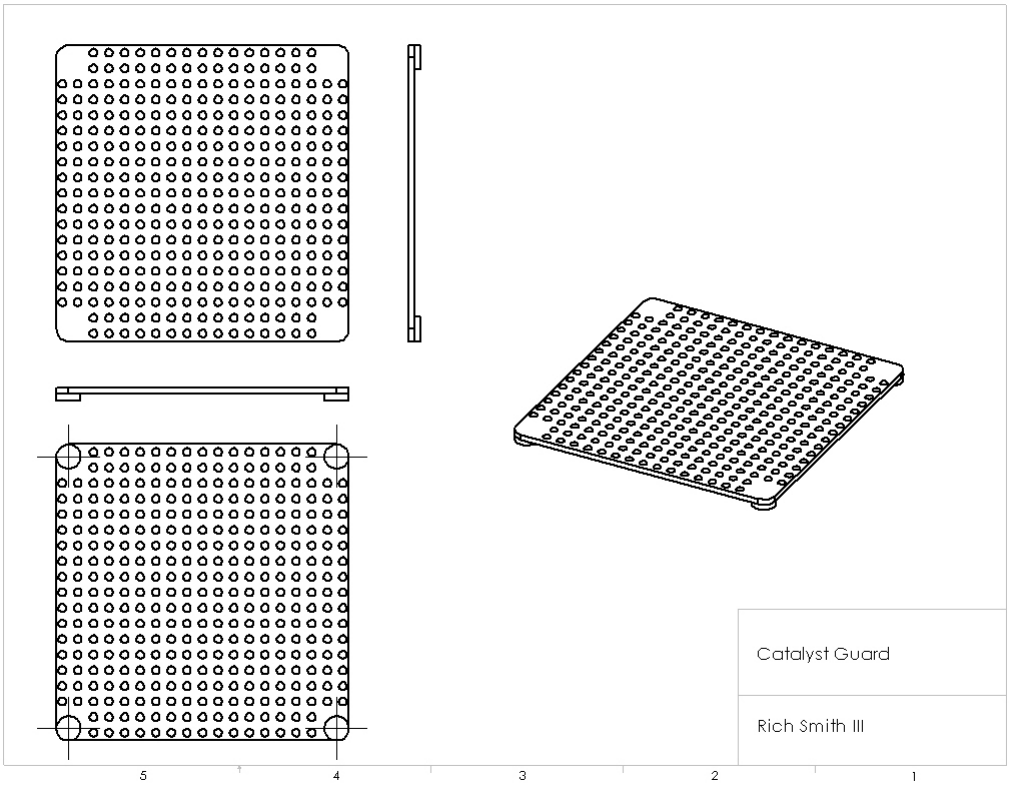

Figure E.1: Computer Aided Drawing of Catalyst Guard

Bibliography

[1] H. Ibrahim, A. Ilinca, and J. Perron. Energy storage systems-Characteristics and comparisons, 2008.

[2] Mildred Dresselhaus. Basic Research Needs for the Hydrogen Economy. *Fuel Cells*, 21:U1084–U1085, 2004.

[3] Marcelo Carmo, David L. Fritz, Jürgen Mergel, and Detlef Stolten. A comprehensive review on PEM water electrolysis. *International Journal of Hydrogen Energy*, 38(12):4901–4934, April 2013.

[4] R. L. Rudnick and S. Gao. Composition of the Continental Crust. In *Treatise on Geochemistry: Second Edition*, volume 4, pages 1–51. 2013.

[5] Daniel V. Schroeder. An Introduction to Thermal Physics, 1999.

[6] Frano Barbir. *PEM fuel cells: theory and practice*. 2005.

[7] William B. Jensen. Faradays laws or Faradays law? *Journal of Chemical Education*, 89:1208–1209, 2012.

[8] David l Fritz. Pem electrolysis diagram, 2013. User created page with UploadWizard.

[9] William Y. Hsu and Timothy D. Gierke. Ion transport and clustering in nafion perfluorinated membranes, 1983.

[10] Kenneth A. Mauritz and Robert B. Moore. State of understanding of Nafion. *Chemical Reviews*, 104:4535–4585, 2004.

[11] Chris Yang, S. Srinivasan, a. B. Bocarsly, S. Tulyani, and J. B. Benziger. A comparison of physical properties and fuel cell performance of Nafion and zirconium phosphate/Nafion composite membranes. *Journal of Membrane Science*, 237:145–161, 2004.

[12] Cristina Neagu, Henri Jansen, Han Gardeniers, and Miko Elwenspoek. Electrolysis of water: An actuation principle for MEMS with a big opportunity. *Mechatronics*, 10:571–581, 2000.

[13] Glyn D Short and Edmund Bishop. Concentration Overpotentials on Antimony Electrodes in Differential Electrolytic Potentiometry. *Analytical Chemistry*, 37:962–967, 1965.

[14] Allen J Bard and Larry R Faulkner. *Electrochemical Methods: Fundamentals and Applications*, volume 677. 2001.

[15] Bruce Averill and Patricia Eldredge. *Chemistry: Principles, Patterns, and Applications*. 2006.

[16] J. Rammer and H. Smith. Quantum field-theoretical methods in transport theory of metals. *Reviews of Modern Physics*, 58:323–359, 1986.

[17] Meng Ni, Michael K H Leung, and Dennis Y C Leung. An electrochemical model of a solid oxide steam electrolyzer for hydrogen production. *Chemical Engineering and Technology*, 29:636–642, 2006.

[18] A D McNaught and A Wilkinson. *IUPAC Compendium of Chemical Terminology (The "Gold Book")*. 2014.

[19] L.M. Peter. Semiconductor electrochemistry, 1988.

[20] H. Wendt and V. Plzak. Electrocatalytic and thermal activation of anodic oxygen- and cathodic hydrogen-evolution in alkaline water electrolysis, 1983.

[21] D. A B Miller, D. S. Chemla, T. C. Damen, A. C. Gossard, W. Wiegmann, T. H.

Wood, and C. A. Burrus. Band-edge electroabsorption in quantum well structures: The quantum-confined stark effect. *Physical Review Letters*, 53:2173–2176, 1984.

[22] S. A. Empedocles. Quantum-Confined Stark Effect in Single CdSe Nanocrystallite Quantum Dots, 1997.

[23] Laurence D. Burke, Oliver J. Murphy, John F. O'Neill, and Srinivasan Venkatesan. The oxygen electrode. Part 2.Behavior at Ruthenium Black Electrodes, 1972.

[24] Laurence D. Burke, Oliver J. Murphy, John F. O'Neill, and Srinivasan Venkatesan. The oxygen electrode. Part 4.Lowering of Overvoltage for Oxygen Elolution at Noble-etal electrodes in presence of Ruthenium salts, 1974.

[25] Laurence D. Burke, Oliver J. Murphy, John F. O'Neill, and Srinivasan Venkatesan. The oxygen electrode. Part 3. Inhibition of Oxygen Evolution Reaction, 1972.

[26] Melvin H. Miles. Evaluation of electrocatalysts for water electrolysis in alkaline solutions, 1975.

[27] S. Trasatti and G. Buzzanca. Ruthenium dioxide: a new interesting electrode material. Solid structure and electrochemical behaviour. *J. Electroanal. Chem. Interfacial Electrochem.*, 29:A1–A5, 1971.

[28] Dario Galizzioli, Franco Tantardini, and Sergio Trasatti. Ruthenium dioxide: a new electrode material. I. Behaviour in acid solutions of inert electrolytes. *Journal of Applied Electrochemistry*, 4:57–67, 1974.

[29] J. K. Nø rskov, T. Bligaard, A. Logadottir, J. R. Kitchin, J. G. Chen, S. Pandelov, and U. Stimming. Trends in the Exchange Current for Hydrogen Evolution. *Journal of The Electrochemical Society*, 152(3):J23, 2005.

[30] Holger Dau, Christian Limberg, Tobias Reier, Marcel Risch, Stefan Roggan, and Peter Strasser. The Mechanism of Water Oxidation: From Electrolysis via Homogeneous to Biological Catalysis, 2010.

[31] Isabela C. Man, Hai Yan Su, Federico Calle-Vallejo, Heine A. Hansen, José I. Martínez, Nilay G. Inoglu, John Kitchin, Thomas F. Jaramillo, Jens K. Nø rskov, and Jan Rossmeisl. Universality in Oxygen Evolution Electrocatalysis on Oxide Surfaces. *ChemCatChem*, 3:1159–1165, 2011.

[32] JC Cruz and V Baglio. Preparation and Characterization of RuO2 Catalysts for Oxygen Evolution in a Solid Polymer Electrolyte. *International . . .*, 6:6607–6619, 2011.

[33] C P Depauli and S Trasatti. Electrochemical Surface Characterization of Iro2+Sno2 Mixed-Oxide Electrocatalysts. *Journal of Electroanalytical Chemistry*, 396:161–168, 1995.

[34] S. Ardizzone, C. L. Bianchi, G. Cappelletti, M. Ionita, A. Minguzzi, S. Rondinini, and A. Vertova. Composite ternary SnO2-IrO2-Ta2O5 oxide electrocatalysts. *Journal of Electroanalytical Chemistry*, 589:160–166, 2006.

[35] Paul Ruetschi and Paul Delahay. Potential at Zero Charge for Reversible and Ideal Polarized Electrodes. *The Journal of Chemical Physics*, 23:697–699, 1955.

[36] Etsushi Tsuji, Akihito Imanishi, Ken Ichi Fukui, and Yoshihiro Nakato. Electrocatalytic activity of amorphous RuO2 electrode for oxygen evolution in an aqueous solution. *Electrochimica Acta*, 56:2009–2016, 2011.

[37] Youngmin Lee, Jin Suntivich, Kevin J May, Erin E Perry, and Yang Shao-Horn. Synthesis and Activities of Rutile IrO2 and RuO2 Nanoparticles for Oxygen Evolution in Acid and Alkaline Solutions. *The Journal of Physical Chemistry Letters*, 3:399–404, 2012.

[38] J. Rossmeisl, Z. W. Qu, H. Zhu, G. J. Kroes, and J. K. Nø rskov. Electrolysis of water on oxide surfaces. *Journal of Electroanalytical Chemistry*, 607:83–89, 2007.

[39] Tobias Reier, Mehtap Oezaslan, and Peter Strasser. Electrocatalytic oxygen evolution reaction (OER) on Ru, Ir, and pt catalysts: A comparative study of nanoparticles

and bulk materials. *ACS Catalysis*, 2:1765–1772, 2012.

[40] Kyu Nam Jung, Ahmer Riaz, Seung Bok Lee, Tak Hyoung Lim, Seok Joo Park, Rak Hyun Song, Sukeun Yoon, Kyung Hee Shin, and Jong Won Lee. Urchin-like α-MnO2 decorated with Au and Pd as a bi-functional catalyst for rechargeable lithium-oxygen batteries. *Journal of Power Sources*, 244:328–335, 2013.

[41] Michael Cross, Walter Varhue, and Thomas Valdez. Structure and electro-catalytic properties of electrode materials consisting of Pt nanorod decorated/RuO2 nanorod coated substrates. *International Journal of Hydrogen Energy*, 37:13256–13262, 2012.

[42] Michael Cross, Walter Varhue, Keith Pelletier, and Michael Stewart. RuO2 nanorod coated cathode for the electrolysis of water. *International Journal of Hydrogen Energy*, 37:2166–2172, 2012.

[43] B. Hammer and J.K. Norskov. Theoretical Surface Science and Catalysis Calculations and Concepts. *Advances in Catalysis*, 45:71–129, 2000.

[44] Germany A.Heinzzel, University of Duisburg-Essen, Duisburg, German F. Mahlendorf, University of Duisburg-Essen, Duisburg, and Germany C. Jansen, University of Duisburg-Essen, Duisburg. Bipolar Plates. *Elsevier*, pages 810–816, 2009.

[45] Colleen Spiegel. *PEM Fuel Cell Modeling and Simulation Using Matlab*. 2008.

[46] D. H. Jeon, S. Greenway, S. Shimpalee, and J. W. Van Zee. The effect of serpentine flow-field designs on PEM fuel cell performance. *International Journal of Hydrogen Energy*, 33:1052–1066, 2008.

[47] Sehkyu Park, Jong Won Lee, and Branko N. Popov. A review of gas diffusion layer in PEM fuel cells: Materials and designs. *International Journal of Hydrogen Energy*, 37:5850–5865, 2012.

[48] R Tunold, E Rasten, and G Hagen. Electrocatalysis in water electrolysis with solid polymer electrolyte. *Electrochimica Acta*, 48:3945–3952, 2003.

[49] Scott D. Greenway, Elise B. Fox, and Amy a. Ekechukwu. Proton exchange membrane (PEM) electrolyzer operation under anode liquid and cathode vapor feed configurations. *International Journal of Hydrogen Energy*, 34(16):6603–6608, August 2009.

[50] Xiao Zi Yuan, Hui Li, Shengsheng Zhang, Jonathan Martin, and Haijiang Wang. A review of polymer electrolyte membrane fuel cell durability test protocols, 2011.

[51] Joshua M. Spurgeon and Nathan S. Lewis. Proton exchange membrane electrolysis sustained by water vapor. *Energy and Environmental Science*, 4(8):2993, 2011.

[52] Rosemary Gene Ehl and Aaron J. Ihde. Faraday's electrochemical laws and the determination of equivalent weights. *Journal of chemical education*, 31:226–232, 1954.

[53] R. García-Valverde, N. Espinosa, and A. Urbina. Simple PEM water electrolyser model and experimental validation. In *International Journal of Hydrogen Energy*, volume 37, pages 1927–1938, 2012.

[54] M. Santarelli, P. Medina, and M. Calì. Fitting regression model and experimental validation for a high-pressure PEM electrolyzer. *International Journal of Hydrogen Energy*, 34:2519–2530, 2009.

[55] M. S. Wilson and S. Gottesfeld. Thin-film catalyst layers for polymer electrolyte fuel cell electrodes. *Journal of Applied Electrochemistry*, 22:1–7, 1992.

[56] Sangil Han, Jang Woo Lee, Chan Kwak, Geun Seok Chai, In Hyuk Son, Moon Yup Jang, Sung Guk An, Sung Yong Cho, Jun Young Kim, Hyung Wook Kim, Alexey Alexandrovych Serov, Youngtai Yoo, and Kie Hyun Nam. High performance membrane-electrode assembly based on a surface-modified membrane. *Journal of Power Sources*, 167:74–78, 2007.

[57] Paul William Majsztrik. *Mechanical and transport properties of Nafion for PEM fuel cells; temperature and hydration effects*. PhD thesis, 2008.

[58] G S Karlberg, J Rossmeisl, and J K Nø rskov. Estimations of electric field effects

on the oxygen reduction reaction based on the density functional theory. *Physical chemistry chemical physics : PCCP*, 9(37):5158–61, October 2007.